THE GEOLOGICAL SOCIETY OF AMERICA®

Mid-Cretaceous thick carbonate accumulation in Northern Lhasa (Tibet): eustatic vs. tectonic control?

Yiwei Xu[1], Xiumian Hu[1,†], Eduardo Garzanti[2], Marcelle BouDagher-Fadel[3], Gaoyuan Sun[4], Wen Lai[1], and Shijie Zhang[5]

[1]*State Key Laboratory of Mineral Deposits Research, School of Earth Sciences and Engineering, Nanjing University, Nanjing 210023, China*

[2]*Department of Earth and Environmental Sciences, Università di Milano-Bicocca, Milano 20126, Italy*

[3]*Department of Earth Sciences, University College London, Gower Street, London, WC1E 6BT, UK*

[4]*College of Oceanography, Hohai University, Nanjing 210098, China*

[5]*School of Tourism, Henan Normal University, Xinxiang 453007, China*

ABSTRACT

Widespread accumulation of thick carbonates is not typical of orogenic settings. During the mid-Cretaceous, near the Bangong suture in the northern Lhasa terrane, the shallow-marine carbonates of the Langshan Formation, reaching a thickness up to ~1 km, accumulated in an epicontinental seaway over a modern area of 132 × 10^3 km^2, about half of the Arabian/Persian Gulf. The origin of basin-wide carbonate deposits located close to a newly formed orogenic belt is not well understood, partly because of the scarcity of paleogeographic studies on the evolution of the northern Lhasa. Based on a detailed sedimentological and stratigraphic investigation, three stages in the mid-Cretaceous paleogeographic evolution of northern Lhasa were defined: (1) remnant clastic sea with deposition of Duoni/Duba formations (Early to early Late Aptian, ca. 125–116 Ma); (2) expanding carbonate seaway of Langshan Formation (latest Aptian–earliest Cenomanian, ca. 116–99 Ma); and (3) closure of the carbonate seaway represented by the Daxiong/Jingzhushan formations (Early Cenomanian to Turonian, ca. 99–92 Ma). Combined with data on tectonic subsidence and eustatic curves, we emphasized the largely eustatic control on the paleogeographic evolution of the northern Lhasa during the latest Aptian–earliest Cenomanian when the Langshan carbonates accumulated, modulated by long-term slow tectonic subsidence and high carbonate productivity.

†Corresponding author: huxm@nju.edu.cn.

INTRODUCTION

The Lhasa terrane, lying between the Indus–Yarlung suture to the south and the Bangong suture to the north (Fig. 1A), is the latest microcontinent accreted to Asia before collision between the Indian and Asian continental margins. The timing of collision between the Qiangtang and Lhasa terranes along the Bangong suture (Fig. 1A) is widely debated (Girardeau et al., 1984; Dewey et al., 1988; Fan et al., 2014; Zhu et al., 2016; Ma et al., 2017; Li et al., 2019). However, it is widely accepted that collision started before the late Early Cretaceous based on: (1) non-marine clastics deposited in the Nima basin between the late Early to early Late Cretaceous (Kapp et al., 2007; Kapp and DeCelles, 2019); and (2) terrigenous detritus supplied to northern Lhasa by the Bangong suture and southern Qiangtang since the late Early Cretaceous (Lai et al., 2019a; Li et al., 2020). During the mid-Cretaceous, the north Lhasa region was thus situated in an orogenic setting where a several-km-thick succession was deposited, including upward-shallowing siliciclastics (Duoni and Duba formations), carbonates (Langshan Formation), and thick conglomerate-bearing deposits (Jingzhushan and Daxiong formations) (Pan et al., 2004; Sun et al., 2015a; Sun et al., 2017; Lai et al., 2019a, 2019b).

The Langshan Formation is the youngest marine unit in the northern Lhasa terrane (Pan et al., 2004), and its occurrence close to an evolving suture zone is unusual for its basin-wide distribution (Fig. 1B) and great thickness (~1 km). Cenozoic carbonates in foreland basins are mostly limited to the distal margin, and with a ribbon-like shape (Bosence, 2005). Moreover, their thickness does not exceed a few hundreds of meters, because carbonate production is hampered in orogenic settings where tectonic uplift and erosion produce abundant terrigenous detritus (Wilson, 1975; Dorobek, 1995). However, in a few cases (e.g., the Papua–New Guinea foreland basin) carbonate thickness may reach 1.2 km (Sinclair, 1997). Finally, carbonates generally occur only in the starved initial stage of foreland-basin deposition (Davies et al., 1989; Sinclair, 1997), whereas the succession mostly consists of siliciclastic, "molasse-type" deposits (Busby and Ingersoll, 1995).

Several scenarios have been envisaged as a framework for deposition of the Langshan Formation, including (1) a back-arc extensional basin (Zhang et al., 2004); (2) a peripheral foreland basin (Leeder et al., 1988; Leier et al., 2007; DeCelles et al., 2007); (3) a retroarc foreland basin (Zhang et al., 2011); and (4) a composite foreland basin (Lai et al., 2019a). Moreover, Leeder et al. (1988) emphasized the role played by eustatic changes in peripheral foreland basins. However, these diverging interpretations are largely based on studies of the mid-Cretaceous clastic strata in the northern Lhasa terrane (Leeder et al., 1988; Leier et al., 2007; Zhang et al., 2011; Sun et al., 2015a, 2017; Lai et al., 2019a, 2019b, Li et al., 2020). In contrast, the 1-km-thick Langshan Formation has been the target of only a few studies on fossil content and depositional age (Scott e al., 2010; Rao et al., 2015; BouDagher-Fadel et al., 2017; Rao et al., 2020). The sedimentology and the paleogeographic context of the Langshan Formation have been poorly investigated so far, and its depositional environment was simply described as either carbonate platform

GSA Bulletin; January/February 2022; v. 134; no. 1/2; p. 389–404; https://doi.org/10.1130/B35930.1; 11 figures; 1 supplemental file.
published online 11 May 2021

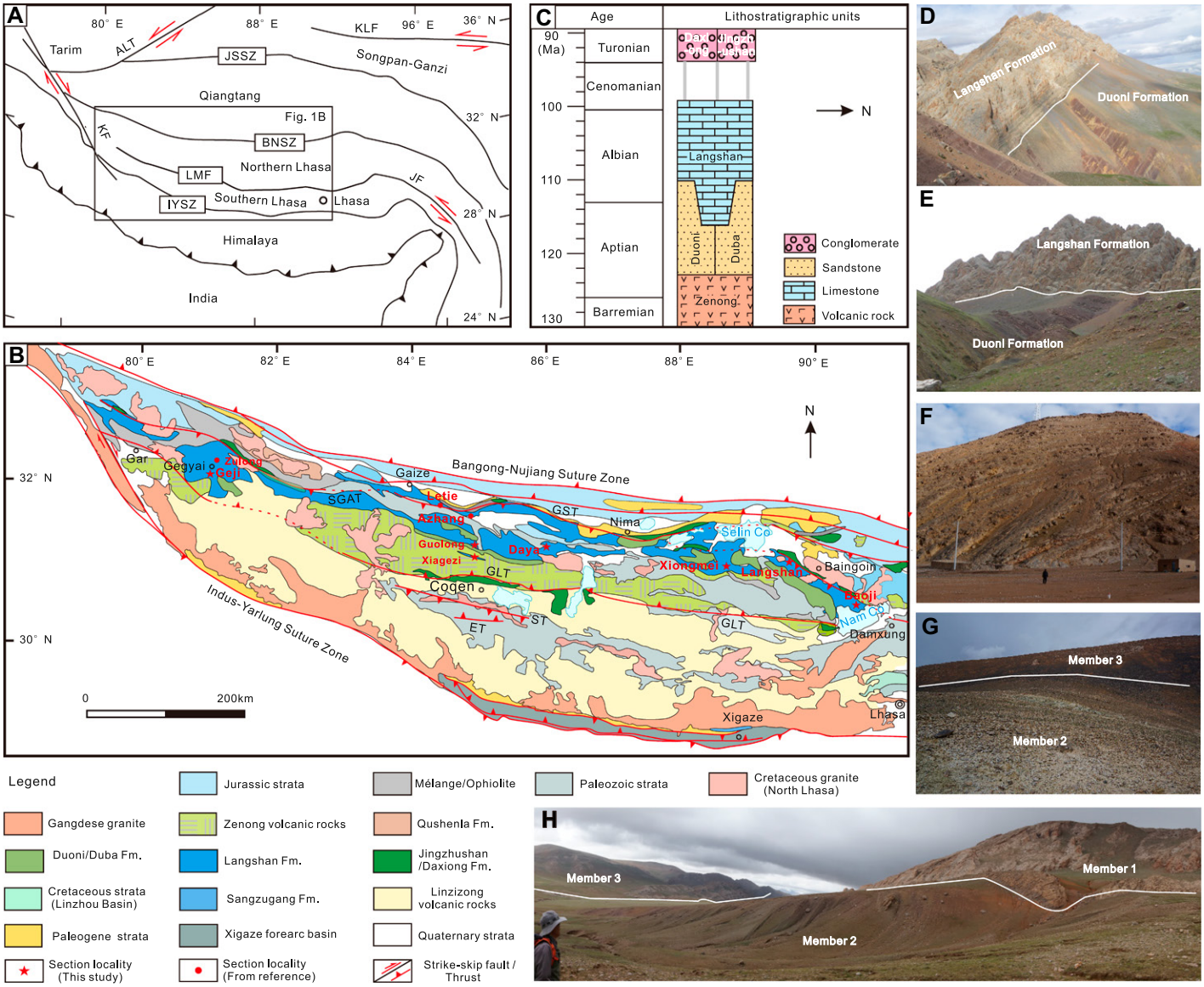

Figure 1. (A) Simplified tectonic map of the Himalaya and Tibet showing major tectonic domains and suture zones (Pan et al., 2004). BNSZ—Bangong–Nujiang suture zone; IYZS—Indus–Yarlung–Zangbo suture; JSSZ—Jinshajiang suture zone; LMF—Luobadui–Milashan fault; JF—Jiali fault; KLF—Kunlun fault; KF—Karakoram fault; ALT—Altyn Tagh fault. (B) Simplified geological map of the Lhasa terrane, showing the studied sections (modified after Pan et al., 2004). GST—Gaize-Selin Co thrust; SGAT—Shiquan–Gaize–Amdo thrust; GLT—Gugu La thrust; ST—Shibaluo thrust; ET—Emei La thrust. Stratigraphic data from northern sections from Xu et al., (2020). (C) Cretaceous strata in the Northern Lhasa terrane. (D) Conformable contact between the Duoni and Langshan formations in the Geren Co area (GPS: 31°20′47.80″N; 88°11′36.81″E). (E) More close observation on conformable contact between the Duoni and Langshan formations in the Geren Co area. (F) Langshan Formation in the Geji section (GPS: 32°27′41.545″N; 80°54′56.108″E). (G) Langshan Formation in the Baoji section (GPS: 30°57′54.85″N; 90°19′33.83″E). (H) Langshan Formation in the Xiongmei section (GPS: 31°19′9.09″N; 88°51′22.38″E). Dip direction and dip angle of members 1, 2, and 3 are 200°/52°, 195°/55° and 195°/50°, respectively.

or carbonate ramp (Leeder et al., 1988; Yu and Wang, 1990; Sun et al., 2017). The lack of information about the Langshan Formation hinders our understanding of its origin and of the paleogeographic evolution of the northern Lhasa terrane.

In order to investigate the origin of the Langshan Formation, we have carried out an integrated stratigraphic, sedimentological, and microfacies analysis of seven stratigraphic sections measured throughout the Langshan Formation in the northern Lhasa terrane. These new data, combined with previous observations, are used to reconstruct the mid-Cretaceous tectonic subsidence and paleogeographic evolution of northern Lhasa and to differentiate the potential controlling factors of this thick and basin-wide carbonate accumulation.

GEOLOGICAL BACKGROUD

The Lhasa terrane is divided into the southern Lhasa and northern Lhasa terranes by the Luobadui–Milashan Fault (Fig. 1A) (Pan et al.,

2004; Kapp and DeCelles; 2019). The southern Lhasa terrane mainly comprises the Xigaze forearc basin and the Gangdese arc, developed during subduction of Neo-Tethyan oceanic lithosphere (Kapp and DeCelles, 2019). The northern Lhasa terrane mainly comprises Paleozoic metasedimentary rocks, Jurassic–Cretaceous sedimentary strata, and Mesozoic igneous rocks (Fig. 1B) (Pan et al., 2004).

Cretaceous Stratigraphy of Northern Lhasa

Cretaceous strata in the northern Lhasa terrane include the Duoni, Duba, Langshan, Jingzhushan, and Daxiong formations (Pan et al., 2004; Sun et al., 2015a; Lai et al., 2019a, 2019b) (Fig. 1C). The Duoni and Duba formations consist of terrigenous clastics sourced from the volcanic rocks of the Zenong Group (Duoni Formation) and from the Bangong suture and southern Qiangtang terrane (Duba Formation) (Leier et al., 2007; Zhang et al., 2011; Sun et al., 2017; Lai et al., 2019a; Li et al., 2020). The depositional ages of these units are constrained as 123–110 Ma based on detrital-zircon chronostratigraphy and age of intercalated volcanic rocks (Leier et al., 2007; Sun et al., 2017; Lai et al., 2019a).

The Langshan Formation conformably overlies the Duoni Formation (Figs. 1D and 1E). The unit is widely distributed in the northern Lhasa terrane with a modern area of $\sim 132 \times 10^3$ km^2, and consists of shallow-marine bioclastic limestone interbedded with sandstone, mudrock, marlstone, tuff, and adakitic volcanic rocks (Sun et al., 2015b, 2017). The Langshan Formation, deposited between the Late Aptian and the Early Cenomanian based on biostratigraphy (BouDagher-Fadel et al., 2017; Xu et al., 2020), is overlain either unconformably or in fault contact by the red pebbly siliciclastics of the Jingzhushan or Daxiong formations. The Jingzhushan Formation, exposed to the north of the Langshan Formation outcrop belt, was chiefly derived from erosion of the Langshan Formation (Lai et al., 2019b). The Daxiong Formation, exposed to the south of the Langshan Formation outcrop belt, was mainly sourced from both the Zenong Group and the Langshan Formation (Sun et al., 2015a). The depositional age of the Jingzhushan and Daxiong formations is constrained at the Turonian (ca. 92 Ma), based on the age of intercalated tuffs (Sun et al., 2015a; Lai et al., 2019b).

METHODS

Microfacies Analysis

Samples were collected from seven measured stratigraphic sections (Fig. 1B) with a sampling frequency of 2–4 m for limestone strata. Limestone beds intercalated with siliciclastic strata were also sampled. A total of 854 thin sections were used for microfacies analysis, performed by examining grain components, textures, and macrofossil and microfossil assemblages. Carbonate rocks were classified based on Dunham (1962) and Embry and Klovan (1971).

Larger Benthic Foraminiferal Biozones

Based on the foraminiferal assemblages studied in thin sections, biozones were identified and correlated to the established Tibetan Larger Benthic Foraminiferal biozones of the Cretaceous according to BouDagher-Fadel et al. (2017). The eight identified foraminiferal biozones (TLK1a–h) are Aptian to early Cenomanian in age, were used to correlate the South Tibetan sedimentary successions (Fig. 2B), and were calibrated against the biostratigraphic time scale and chronostratigraphy as defined by Gradstein et al. (2012). For additional details about biozone subdivisions, see BouDagher-Fadel et al. (2017).

Tectonic Subsidence Analysis

The reconstruction of tectonic-subsidence curves was based on stratigraphy of the Duoni, Duba, Langshan, and Jingzhushan formations. The ages of the Duoni/Duba and Jingzhushan formations, constrained by U-Pb dating of zircon crystals in tuffs and zircon grains in sandstones, are from published data (Sun et al., 2017; Lai

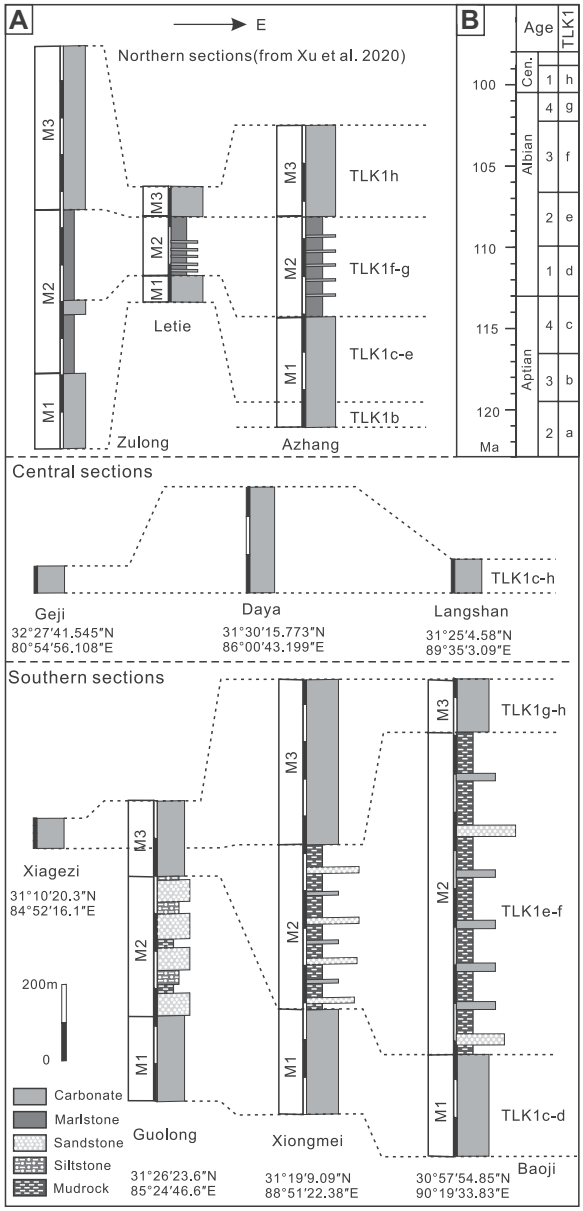

Figure 2. (A) Lithology and biostratigraphic correlation (data for northern sections and Xiagezi section from Xu et al., 2020, and BouDagher-Fadel et al., 2017). (B) Larger benthic foraminiferal biozones and corresponding ages (modified after BouDagher-Fadel et al., 2017). Cen.—Cenomanian; TLK1—Tibetan Larger foraminiferal zones of the Cretaceous, M1—member 1; M2—member 2; M3—member 3.

et al., 2019a, 2019b). The age of the Langshan Formation is constrained by larger benthic foraminiferal biozones (BouDagher-Fadel et al., 2017; Xu et al., 2020; and this study). Following standard backstripping procedures (Allen and Allen, 2005), strata were first decompacted based on the relationship between porosity and depth empirically derived from the study of eight wells in the North Sea (Sclater and Christie, 1980). Next, the effect of sediment load was removed based on Airy isostatic balance. Paleowater depth was estimated based on microfacies analysis. Correction for global eustasy was based on Miller et al. (2005). The tectonic subsidence curve was generated with BasinMod1-D software (provided by Platte River Associates; www.platte.com). Data on which the analysis was made are provided in Table S1 of Supplementary Materials[1].

STRATIGRAPHY

Lithostratigraphy

The characterization of the Langshan Formation was relied on the seven sections newly measured in this work (Baoji, Xiongmei, Guolong, Xiagezi, Langshan, Daya, and Geji sections) and on three sections reported in Xu et al. (2020) (Azhang, Letie and Zulong sections). Three areas were identified: (1) south: Baoji, Xiongmei, Guolong, and Xiagezi sections, located at the southern edge of the Langshan Formation outcrop belt; (2) center: Langshan, Daya, and Geji sections; and (3) north: Azhang, Letie, and Zulong sections exposed along the northern edge of the Langshan Formation outcrop belt (Fig. 2A).

In the southern area (Baoji, Xiongmei, and Guolong sections), the Langshan Formation can be subdivided into three informal members based on lithology. Member 1 comprises massive bioclastic limestone, with a thickness of 412 m in the Baoji section, 271 m in the Xiongmei section, and 235 m in the Guolong section. Member 2 comprises red to green mudrock interbedded with sandstone and limestone over a thickness of 720 m in the Baoji section and 661 m in the Xiongmei section (Figs. S1 and S2; see footnote 1). In the Guolong section, sandstone is interbedded with tuffs and limestones over a thickness of 400 m (Fig. 2A). Member 3 comprises massive bioclastic limestone with a thickness of 119 m in the Baoji section, 446 m in the Xiongmei section, and 200 m in the Guolong section (Figs. 2A, S1, and S2). All stratigraphic contacts between members are conformable (Figs. 1G and 1H). In the Xiagezi section, the Langshan Formation is characterized by 67 m of bioclastic limestone (Fig. S6; see footnote 1).

In the central area, the Langshan Formation consists of bioclastic limestone without any siliciclastics, and volcanic rocks. In the Daya section, the 219-m-thick lower part is characterized by orbitolinids and the 68-m-thick upper part by rudists (Fig. S4; see footnote 1). The 77-m-thick Langshan section exposes orbitolinid limestone, whereas thin- to medium-bedded bioclastic limestones are 80 m thick in the Geji section (Figs. 1F and S5; see footnote 1).

In the three sections described by Xu et al. (2020) in the northern area, the Langshan Formation can also be subdivided into three informal members. Members 1 and 3 consist of massive bioclastic limestone, whereas member 2 comprises gray marlstone containing calcispheres and planktonic foraminifers interbedded with thin limestone (Xu et al., 2020) (Fig. 2A).

Biostratigraphy

The biostratigraphy of the Guolong and Xiagezi sections in the southern area is described in detail in BouDagher-Fadel et al. (2017). In the present study, we shall mainly focus on the other southern and central sections, where orbitolinid limestones is widely exposed. Further details on paleontological determinations are provided in Plate 1 and Figs. S1–S5 of the Supplementary Material.

In the Baoji section of the southern area, the lower part of member 1 contains *Palorbitolina lenticularis*, *Daxia minima*, and *Sabaudia capitata,* indicating an Aptian 4 age (TLK1c). In the upper part of member 1, the occurrence of *Stomatostoecha plummerae* and *Vercorsella camposauri* indicates an Albian 1 age (TLK1d). The occurrence of *Palorbtolinoides hedini* in the lower part of member 2 indicates an Albian 2 age (TLK1e). The upper part of member 2 contains *Mesorbitolina aperta*, indicating an Albian 3 age (TLK1f). *Praeorbitolina* cf. *wienandsi* appears at the base of member 3, indicating an Albian 4 age (TLK1 g). The occurrence of *Orbitolina qatarica* in member 3 indicates a Cenomanian 1 age (TLK1 h) (Fig. S1 and Plate 1).

In the Xiongmei section of the southern area, the lower part of member 1 contains *Palorbitolina lenticularis*, *Vercorsella arenata*, and *Mesorbitolina parva*, indicating an Aptian 4 age (TLK1c). In member 2, the occurrence of *Palorbtolinoides hedini* and *Mesorbitolina aperta* indicates an Albian 2–3 age (TLK1e-f). Considering the conformable relationship between members 1 and 2, the age of member 1 is Aptian 4–Albian 1. The lower part of member 3 contains *Praeorbitolina* cf. *wienandsi*, *Conicorbitolina* cf. *cuvillieri*, and *Nezzazatinella picardi*, indicating an Albian 4 age (TLK1 g). The occurrence of *Daxia cenomana* and *Orbitolina qatarica* in the middle and upper parts of member 3 indicates a Cenomanian 1 age (TLK1 h) (Fig. S2 and Plate 1).

In the Langshan section of the central area, *Vercorsella arenata* appears in the lower part, indicating an Aptian 4 age (TLK1c). In the middle part, the occurrence of *Palorbtolinoides hedini*, *Mesorbitolina aperta* and *Praeorbitolina* cf. *wienandsi* indicates an Albian 1–Albian 4 age (TLK1d-g). The occurrence of *Orbitolina qatarica* and *Daxia cenomana* in the upper part indicates a Cenomanian 1 age (TLK1 h) (Fig. S3 and Plate 1; see footnote 1).

In the Daya section of the central area, the association of *Daxia minima*, *Vercorsella arenata*, and *Sabaudia capitata* in the lower part indicates an Aptian 4 age (TLK1c). The occurrence of *Palorbtolinoides hedini*, *Cuneolina parva*, and *Mesorbitolina aperta* in the middle part indicates an Albian age. The upper part contains *Daxia cenomana* and *Orbitolina qatarica*, indicating a Cenomanian 1 age (TLK1 h) (Fig. S4 and Plate 1).

In the Geji section of the central area, *Vercorsella arenata* and *Mesorbitolina texana* appear at the base of the Langshan Formation, indicating an Aptian 4 age (TLK1c). The lower part contains *Stomatostoecha plummerae* and *Vercorsella camposaurii*, indicating an Albian 1 age (TLK1d). The middle part contains *Palorbtolinoides hedini* and *Cuneolina parva*, indicating an Albian 2 age (TLK1e). The presence of *Mesorbitolina aperta* and *Conicorbitolina* cf. *cuvillieri* in the upper part indicates an Albian 3 age (TLK1f). The appearance of *Praeorbitolina* cf. *wienandsi* in the uppermost part indicates an Albian 4 age (TLK1 g), and the occurrence of *Daxia cenomana* at the top of the unit indicates a Cenomanian 1 age (TLK1 h) (Fig. S5 and Plate 1).

In summary, the Langshan Formation is dated as Aptian 4–Cenomanian 1 in most southern, central, and northern sections. In the southernmost Xiagezi section, depositional age is restricted to Albian 4–Cenomanian 1 (BouDagher-Fadel et al., 2017), and in the Azhang section, the age is Aptian 3–Cenomanian 1 (BouDagher-Fadel et al., 2017). Members 1–3 were deposited diachronously in southern sections: member 2 is Albian 2–3 in the Baoji and Xiongmei sections, but Albian 1 in the Guolong section (BouDagher-Fadel et al., 2017) (Fig. 2A).

[1]Supplemental Material. Biozones of the Baoji, Xiongmei, Xiagezi and other central sections, and stratigraphic data used to reconstruct tectonic subsidence of the north Lhasa. Please visit https://doi.org/10.1130/GSAB.S.14239910 to access the supplemental material, and contact editing@geosociety.org with any questions.

MICROFACIES OF THE LANGSHAN FORMATION

The 19 microfacies (hereafter MF), were recognized from the seven studied sections of the Langshan Formation. Five depositional environments (patch reef, open lagoon, shallow lagoon, tidal flat, and delta plain) were identified.

Patch Reef

MF1 Coral Packstone

This microfacies, mainly distributed in the Xiongmei and Guolong sections, contains 50%–75% carbonate grains (50%–60% coral debris, partly bored by microorganism and bivalves). Bivalves and peloids are subordinate (10%–15%) (Fig. 3A).

In the Cretaceous, corals dwelled in relatively deeper water than rudists (Gili et al., 1995; Fernández-Mendiola et al., 2013). In the Xiongmei and Guolong sections, this microfacies is interbedded with rudist-rich beds and is thus interpreted as deposited in patch reef to fore-reef environments.

MF2 Red Algae-Rudist Wackestone-Packstone

This microfacies, mainly occurring in the Guolong section and interbedded with MF1, contains 35%–80% carbonate grains, dominated by red algae, rudists, and other bivalves (30%–70%) commonly displaying a micritic envelope. The occurrence of echinoderms is minor (5%–10%) and benthic foraminifers are rare (Fig. 3B).

Red algae occur within the euphotic zone, indicating a shallow-water environment. Considering its relationship with MF1, this microfacies is interpreted as deposited in a patch-reef-related environment.

MF3 Rudist Packstone-Rudstone

This microfacies, interbedded with MF1 and MF2 in the Guolong and Xiongmei sections,

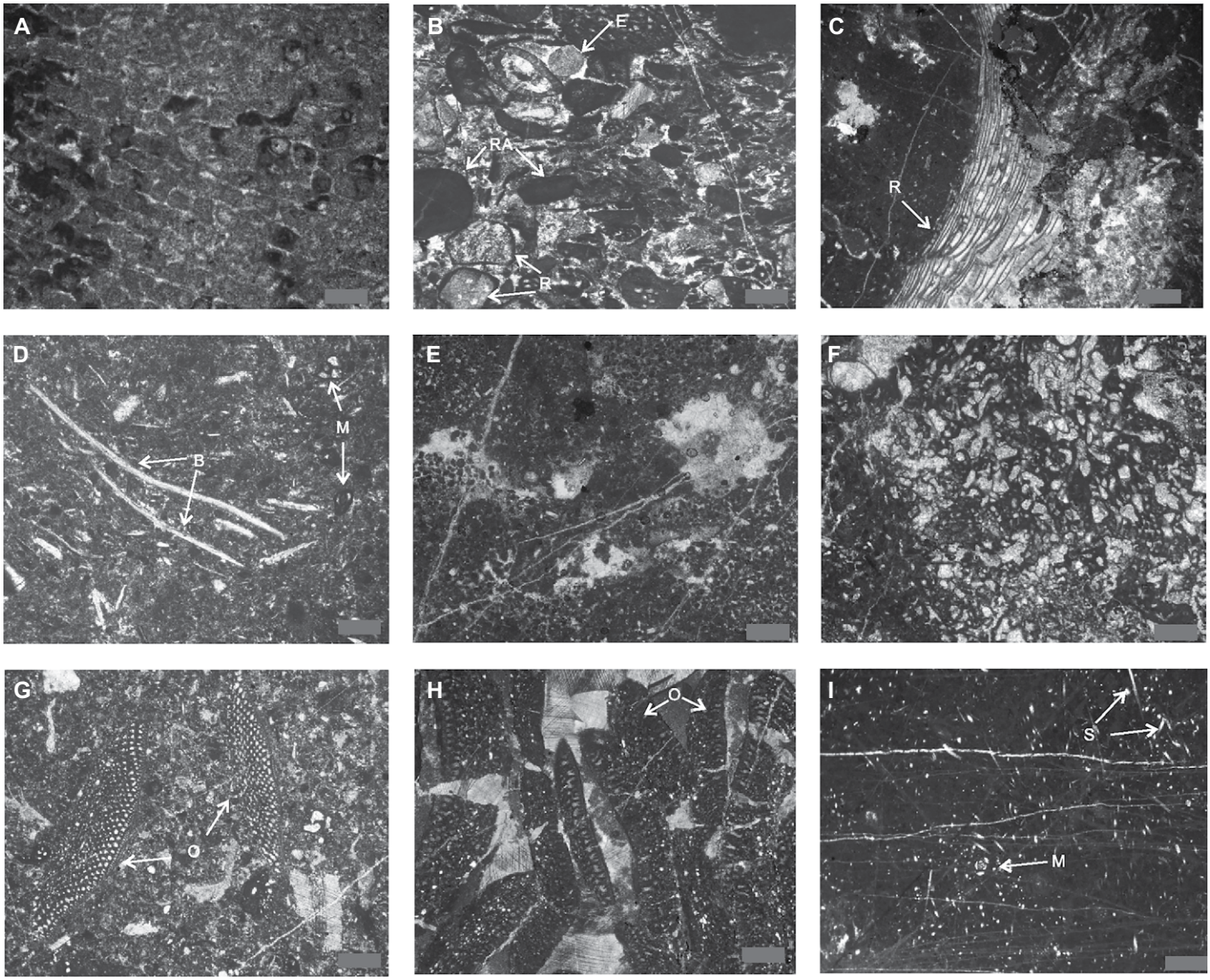

Figure 3. (A) MF1 Coral packstone, 16XM39. (B) MF2 Red algae-rudist wackestone–packstone, 13GL155. (C) MF3 Rudist packstone-rudstone, 16XM59. (D) MF4 Bivalve wackestone, 16XM24. (E) MF5 Peloid packstone, 13GL159. (F) MF6 *Bacinella* boundstone, 13GL194. (G) MF7 Orbitolinid wackestone-packstone, 13GL179. (H) MF8 Orbitolinid packstone-grainstone, 16LS22. (I) MF9 Calcareous spicule wackestone, 17DY07. B—bivalve; E—echinoderm; M—miliolid; O—orbitolinid; R—rudist; RA—red algae; S—sponge spicule. Scale bar = 1 mm.

contains 70%–80% carbonate grains, mostly represented by angular and bored rudist debris (60%–70%) with a diameter of 0.3–2 mm and locally encrusted by *Lithocodium* and *Bacinella*. The occurrence of bivalves and orbitolinids is minor (10%) (Fig. 3C). Red algae, gastropods, echinoderms, and green algae are rare.

Rudists were typical shallow-water reef biota in the Cretaceous (Masse, 1992) forming build-ups together with corals (Masse et al., 1981). Angular rudist debris indicates a short transport distance. This microfacies testifies to a patch-reef environment.

MF4 Bivalve Wackestone

This microfacies, mainly distributed in all sections besides the Langshan and Xiagezi sections, contains 30% carbonate grains, mostly represented by bivalves (25%) with diameters of 0.3–2 mm. The bivalves comprise *Chondrodonta*, oysters, and rudists commonly encrusted by *Lithocodium* and *Bacinella*. The occurrence of orbitolinids (5%), small benthic foraminifers (3%), and green algae (2%) is minor. Red algae and echinoderms are rare (Fig. 3D).

The *Chondrodonta* dwelled in reef or lagoonal environments (Jordan et al., 1985; Di Stefano and Ruberti, 2000) and micritic matrix encasing small benthic foraminifers and green algae indicates low energy and shallow water. A back-reef environment is thus indicated.

Open Lagoon

MF5 Peloid Packstone

This microfacies, interbedded with MF1, MF3, and MF4 in the Xiongmei and Guolong sections, contains 60%–70% carbonate grains, mostly represented by peloids (60%). The occurrence of other bioclasts (orbitolinids, bivalves, benthic foraminifers, and sponge spicules) is minor (5%) (Fig. 3E). Geopetal and thrombolitic structures occur. This facies indicates a back-reef lagoonal environment.

MF6 Bacinella Boundstone

This microfacies, mainly distributed in member 1 of the Guolong section and interbedded with MF5 and MF7, is characterized by *Bacinella* with sparite infill (Fig. 3F). The occurrence of *Bacinella* indicates a reef crest or lagoonal environment (Stein et al., 2012; Kaya and Altıner, 2015).

MF7 Orbitolinid Wackestone-Packstone

This microfacies, distributed in all sections besides the Baoji, Langshan, and Daya sections, contains 20%–60% carbonate grains, mostly represented by well-preserved conical and discoidal orbitolinids (10%–50%) (Fig. 3G). Peloids are common. Bivalve debris and green algae are minor (10%). Rare calcareous spicules, small benthic foraminifers, and terrigenous silt occur.

Orbitolinids lived in shallow waters (10–50 m) (Banner and Simmons, 1994), and their micritic matrix indicates a low-energy state. This microfacies is never flanked by deep-water deposits in this study and is thus interpreted to have been deposited in an open lagoon.

MF8 Orbitolinid Packstone-Grainstone

This microfacies, mainly identified in the Langshan section, contains 70%–80% carbonate grains, mostly represented by oriented, rounded, and densely packed discoidal orbitolinids (70%–75%) partly encrusted by *Bacinella* (Fig. 3H). The occurrence of gastropods and echinoderms is minor (5%).

The rounded and oriented orbitolinids indicate a relative high-energy state, suggesting a shoal environment within a lagoon.

Shallow Lagoon

MF9 Calcareous Spicule Wackestone

This microfacies, mainly distributed in the Daya and Geji sections, contains 15%–30% grains. Calcareous sponge spicules (10%–20%) are associated with orbitolinids, miliolids, bivalves, and small benthic foraminifers (5%–10%) (Fig. 3I).

In contrast with siliceous sponge spicules, which occur in basinal environments (Wilson 1975), calcareous sponge spicules suggest a shallow-water environment (James and Jones, 2015). This microfacies is interbedded with strata containing green algae and small benthic foraminifers. A shallow lagoon environment is thus inferred, in analogy with microfacies FZ-7 in Bachmann and Hirsch (2006).

MF 10 Green algae Wackestone-Packstone

This microfacies, mainly distributed in the Baoji, Langshan, Geji, and Xiagezi sections, contains 30%–70% carbonate grains, mostly well-preserved green algae (dasycladaceans and *Halimeda*) (20%–50%) locally showing a micritic envelope. The occurrence of orbitolinids, bivalves, and echinoderms is minor (15%). Miliolid and textulariid foraminifers occur (3%–5%). Gastropods and calcareous spicules are rare (Fig. 4A).

Dasycladaceans live at euphotic water depths (5–10 m; Banner and Simmons 1994). Green algae are well preserved, suggesting they are in situ or transported over a short distance. A shallow and low-energy lagoonal environment is suggested.

MF11 Orbitolinid Wackestone with Small Benthic Foraminifers

This microfacies, mainly distributed in the Guolong, Xiongmei, and Baoji sections, contains 15%–30% carbonate grains, mostly orbitolinids (10%–20%). The occurrence of miliolids and textulariids is minor (5%–10%). Some dasycladaceans and bivalves occur (5%) (Fig. 4B).

The occurrence of small benthic foraminifers suggests that MF11 was deposited in a shallower environment than MF7, plausibly a shallow lagoon.

MF12 Small Benthic Foraminifera Mudstone-Wackestone

This microfacies, distributed in all sections besides the Langshan section, contains 5%–20% carbonate grains, including various kinds of small benthic foraminifera (5%–15%). Locally micritized miliolids and textulariids are common. The occurrence of green algae is minor (5%). Gastropods, echinoderms, and calcareous spicules are rare (Fig. 4C).

Abundant small benthic foraminifera indicate a shallow lagoon environment with water depth not exceeding 10 m (Davies et al., 2002; Ghabeishavi et al., 2010).

MF13 Bioclastic Grainstone

This microfacies, mainly distributed in the Guolong, Xiongmei, Baoji, and Xiagezi sections, contains 70% carbonate grains, mostly oriented bivalves (50%–60%). Peloids are common (10%–20%) and the occurrence of intraclasts is minor (Fig. 4D). The lack of micrite and oriented bioclasts indicate high-energy conditions in a shoal within a shallow lagoon.

Tidal Flat

MF14 Oncoid Rudstone

This microfacies, mainly occurring at the base of member 3 in the Guolong section in erosional contact with underlying siltstones, contains 70% carbonate grains, mostly symmetrical laminated oncoids, with a diameter of 8 cm at the base of the bed and decreasing upwards of 1–3 cm (Fig. 4E).

Oncoids are indicators of low intertidal to shallow subtidal environments (Flügel, 2010). The MF14 overlies an erosion surface at the base of member 3, interpreted as the base of a transgressive sequence in shallow subtidal to intertidal environments.

MF15 Red and Green Mudrock

Alternating red and green marly mudrocks intercalated with thin siltstone, sandstone, limestone, and sandy limestone layers characterize the Xiongmei section (Fig. 4F). Green mudrocks

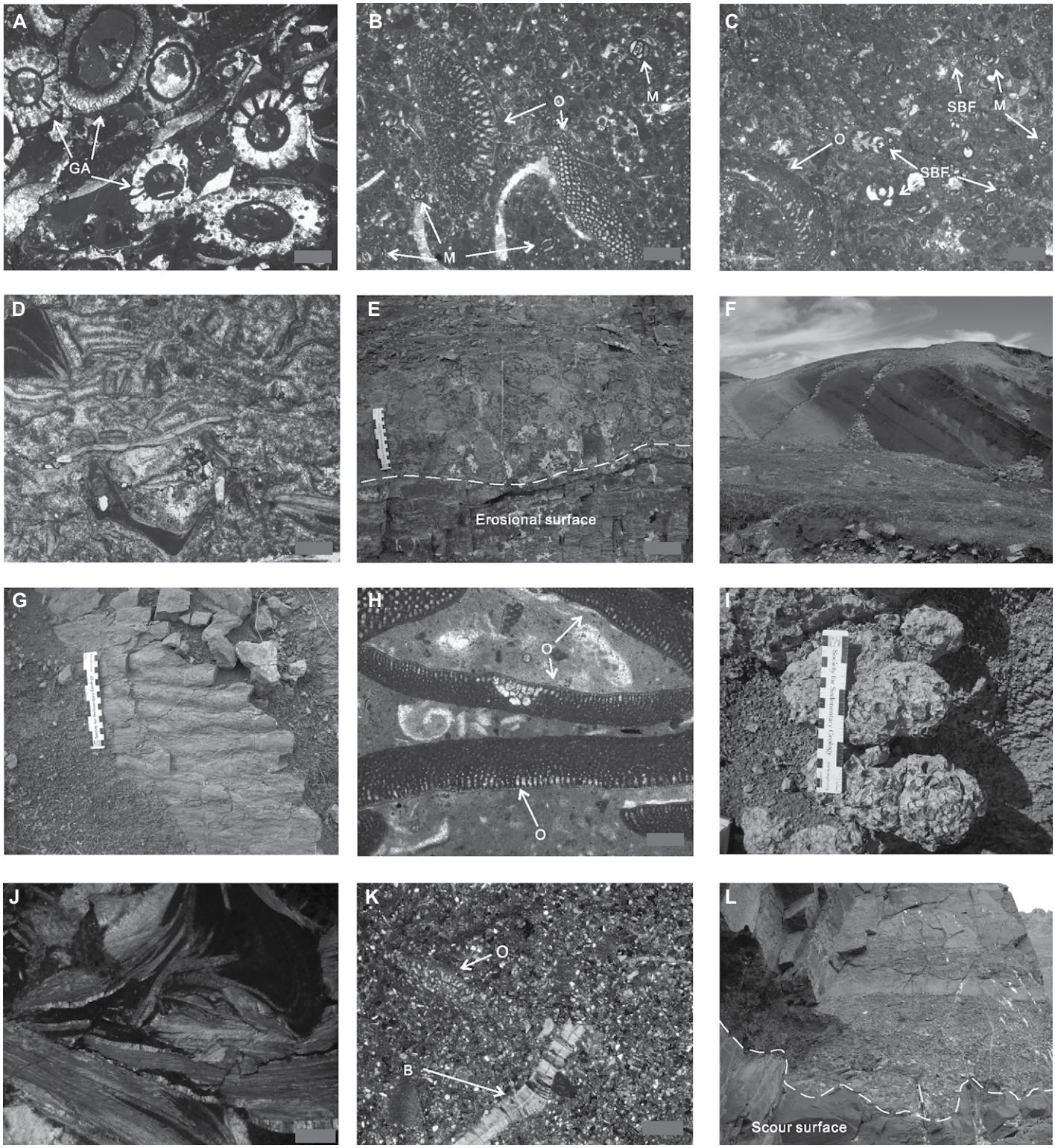

Figure 4. (A) MF10 Green algae wackestone-packstone, 16XM143. (B) MF11 Orbitolinid wackestone with small benthic foraminifers, 16XM157. (C) MF12 Small benthic foraminifer mudstone-wackestone, 16XM219. (D) MF13 Bioclastic grainstone, 16XM138. (E) MF14 Oncoid rudstone (base of member 3, Guolong section). (F) MF15 Red and green mudrocks (member 2, Xiongmei section). (G) Wave ripples (member 2, Xiongmei section). (H) MF16 Discoidal orbitolinid packstone/floatstone, 16XM74. (I) MF17 Oyster packstone (member 2, Xiongmei section). (J) MF17 Oyster packstone, 16XM105. (K) MF18 Sandy bioclastic wackestone, 16XM101. (L) Microconglomerate lenses (member 2, Guolong section). B—bivalve; GA—green algae; M—miliolid; O—orbitolinid; SBF—small benthic foraminifer. Scale bar = 1 mm.

dominate instead in the Baoji section. Wavy bedding and symmetrical ripples occur in both sandstone and bioclastic limestone beds (Fig. 4G).

A red color suggests a subaerial oxic environment, whereas a green color suggests weakly reducing environment. Together with wave ripples, this indicates deposition in peri-tidal environments characterized by different and varying redox conditions.

MF16 Discoidal Orbitolinid Packstone/ Floatstone

This microfacies, mainly found in member 2 of the Xiongmei and Baoji sections and interbedded with MF15 (Figs. 5 and 6), contains 60%–70% carbonate grains, mostly discoidal orbitolinids with test locally including quartz grains set in mixed micrite and terrigenous mud (Fig. 4H).

The occurrence of micrite mixed with silt and clay, and the discoidal form of orbitolinids suggesting adaptation to turbid waters (Pittet et al., 2002), indicates a low-energy, terrigenous-influenced intertidal environment.

MF17 Oyster Packstone

This microfacies, mainly occurring in member 2 of the Xiongmei and Baoji sections and intercalated with MF15 in centimetric layers (Figs. 5 and 6), contains 60%–80% carbonate grains, mostly represented by well-preserved oysters (60%–70%). The occurrence of ooids is minor (10%). Silt-sized quartz grains occur (Figs. 4I and 4J). An intertidal environment is suggested by association with MF15.

MF18 Sandy Bioclastic Wackestone

This microfacies, mainly occurring in member 2 of the Xiongmei and Baoji sections and intercalated with MF15 in centimetric layers (Figs. 5 and 6), contains subequal amounts (20%–30% each) of silt- to sand-sized quartz grains and carbonate allochems. Oysters, green algae, orbitolinids, and ooids are common (Fig. 4K). Wave ripples were observed in the field.

Green algae and ooids indicate shallow water. An intertidal environment is suggested by association with MF15.

Delta Plain

MF19 Coarse-Grained Clastics

This microfacies, occurring only in the Guolong section, consists of red and green lensoid sandstone interbedded with green mudrock, conglomerate, and limestone. The limestone interval contains orbitolinids, oncoids, and bivalves. Up to 10-m-thick sandstone intervals display parallel and tabular oblique lamination. Conglomerate intervals begin with a basal scour surface and may fine upward to sandstone (Fig. 4L).

Lenticular conglomerates and sandstones with parallel and oblique lamination indicate deposition by fluvial currents, whereas interbedded limestones indicate marine deposition. Deposition in a fan delta, including distributary-channels, delta-plain, and marine prodelta environments is suggested.

TECTONIC SUBSIDENCE

The mid-Cretaceous tectonic subsidence history of northern Lhasa can be subdivided into three stages.

Stage 1 (Aptian 1–3, ca.123–116 Ma). During deposition of the Duoni and Duba formation, tectonic subsidence rate for the Duoni Formation is calculated to be ~107 m/m.y. in the Guolong section at the southern edge of the Langshan Formation outcrop belt and ~175 m/m.y. in the Azhang section at the northern edge. In the central area (near Baingoin, DB02 section in Lai et al., 2019a), instead, the rate of tectonic subsidence calculated for Duba Formation in the Langshan section is only ~42 m/m.y. (Fig. 7).

Stage 2 (Aptian 4-Cenomanian 1, ca. 116–99 Ma). During deposition of the Langshan Formation, tectonic subsidence rate was much reduced, and calculated to be ~20 m/m.y. and 37 m/m.y. in the southern Guolong and Xiongmei sections, respectively. Tectonic subsidence was 13 m/m.y. in the northern Azhang section, whereas analysis of central section suggests tectonic inversion and uplift rate of 1.7 m/m.y. (Fig. 7).

Stage 3 (Early Cenomanian to Early Turonian, ca. 99–92 Ma). During deposition of the Jingzhushan Formation, tectonic inversion became generalized, with calculated average uplift rate around 16 m/m.y. (Fig. 7).

DISCUSSION

Paleo-Environmental Evolution of the Langshan Formation

Based on new biostratigraphic and microfacies analysis of seven sections and the three northern sections described in Xu et al. (2020), the paleo-environmental evolution recorded by the Langshan Formation can be subdivided into three phases (Fig. 8).

(1) Aptian 4–Albian 2 (116–107 Ma). During Aptian 4 in the southern sections, member 1 of the Baoji section is dominated by MF2, MF3, and MF11–12, indicating deposition in a shallow lagoon (Fig. 6). In the Xiongmei and Guolong sections, microfacies MF1 to MF7 indicate instead a patch-reef to open-lagoon environment (Fig. 5). In the central sections, microfacies MF8 to MF12 testify to orbitolinids shoals and shallow lagoons (Fig.S3–S5). The northern sections document shallow lagoons and rudist banks (Xu et al., 2020).

During Albian 1–2, microfacies MF14 to MF19 dominate in the southern sections, indicating a tidal flat–delta plain environment (Figs. 5 and 6), whereas sedimentation in shoals to shallow lagoons is documented in the central and northern sections (Figs.S3–S5). A tidal flat in the south transitioning to an open lagoon in the north indicates deposition on a northward-deepening carbonate ramp (Fig. 8).

(2) Albian 3–Albian 4 (ca. 107–100 Ma). During Albian 3 in southern sections, tidal-flat deposition continued in the Baoji and Xiongmei sections, as documented by microfacies MF15 to MF18 (Figs. 5 and 6), whereas MF7 and MF11–MF12 in the Guolong section are indicative of shallow lagoonal environments (Fig. 5). In northern sections, marlstones with abundant calcispheres and planktonic foraminifers overlie the rudist banks (Xu et al., 2020), indicating open-marine sedimentation.

During Albian 4 in the southern sections, microfacies MF2–MF3 and MF11–MF12 characterize the Baoji and Xiongmei sections, indicating patch-reefs to shallow lagoons (Figs. 5 and 6). Shallow lagoonal environments are indicated also in the Xiagezi section, characterized by microfacies MF12 (Fig.S6). Open-marine sedimentation continued in the northern sections (Xu et al., 2020). During Albian 3–4, the central sections are dominated by shallow lagoonal microfacies MF9 to MF12 (Figs.S3-S5). In this time interval, facies distribution documents drastic deepening from shallow-lagoon and rudist-bank to open-marine environments in the north, whereas environmental conditions did not change significantly in central and southern regions. This indicates a flat-topped platform morphology passing rapidly northward to a basin rather than a gently sloping ramp. During Albian 3–4, therefore, the Langshan Formation deposited in a carbonate rimmed platform environment (Fig. 8).

(3) Cenomanian 1 (ca. 100–99 Ma). The southern and central sections are dominated by lagoonal microfacies MF10–MF12 (Figs. 5, 6, and S3–S6), whereas northern sections indicate transition from open-marine to rudist-bank and shallow-lagoon environments (Xu et al., 2020). Langshan Formation carbonates at this time were deposited in a wide shallow lagoon extending from south to north (Fig. 8).

Mid-Cretaceous Paleogeography of Northern Lhasa

Based on stratigraphic and microfacies analysis of the Langshan Formation carried out in this study and combined with previous work, the

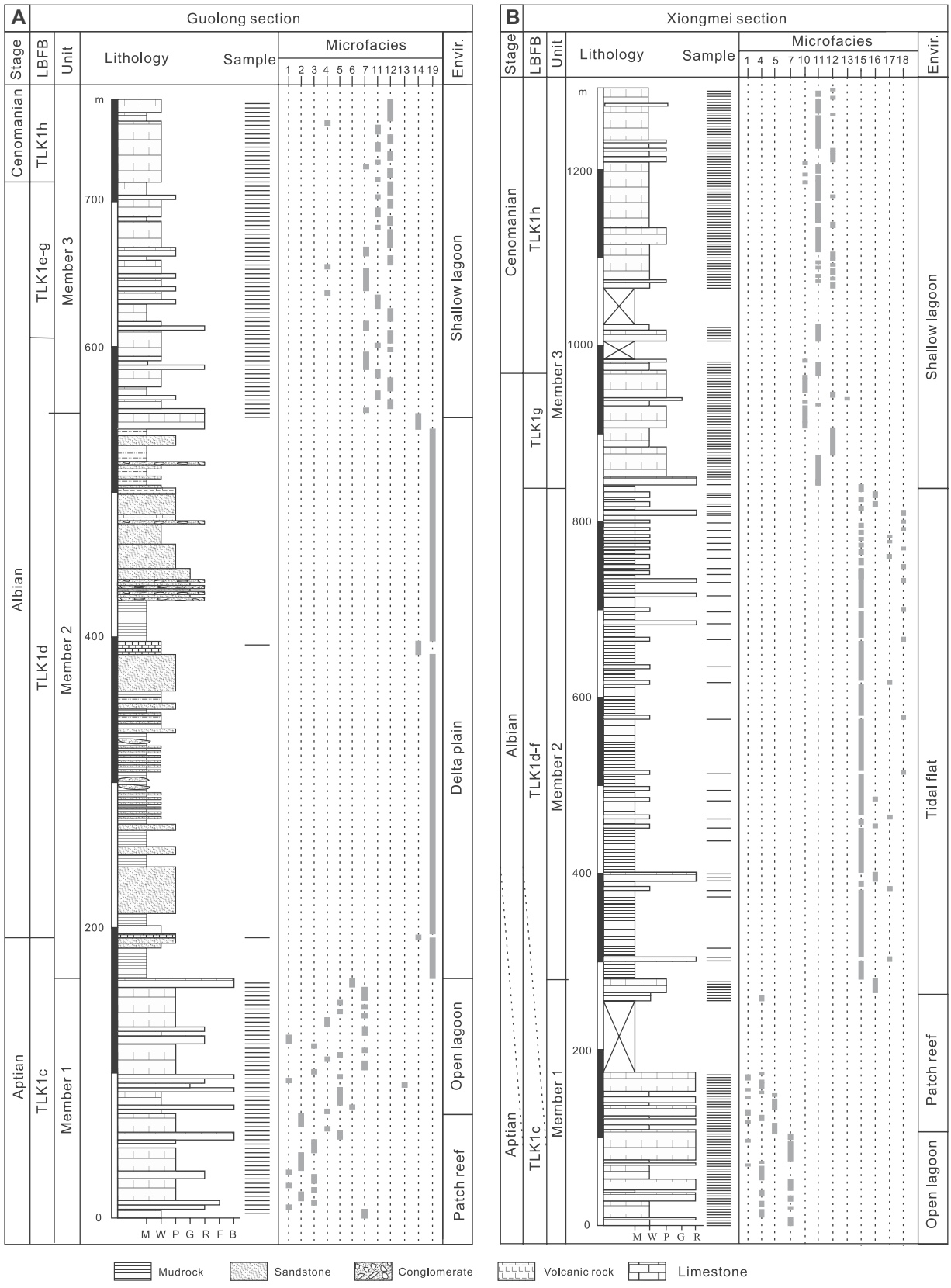

Figure 5. Stratigraphy of the Langshan Formation and microfacies distribution in the (A) Guolong and (B) Xiongmei sections. See text for descriptions of microfacies MF1 to MF19, Envir.—environment; LBFB—larger benthic foraminifera biozone.

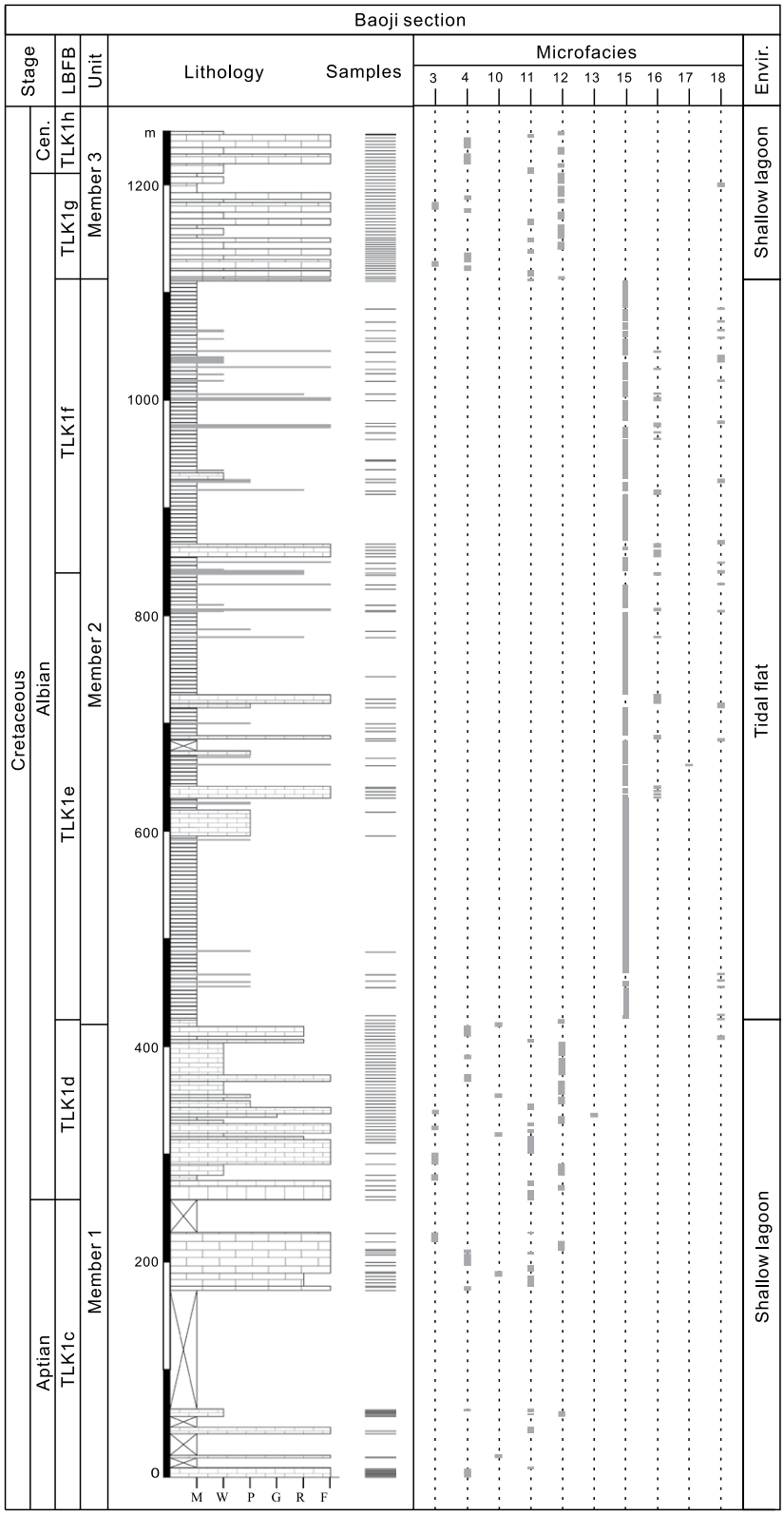

Figure 6. Stratigraphy of the Langshan Formation and microfacies distribution in the Baoji section. Limestone beds are highlighted by thin gray bars to the right of the stratigraphic column. See text for descriptions of microfacies MF1 to MF19. Cen.—Cenomanian; Envir.—environment; LBFB—larger benthic foraminifera biozone. Legend shown in Figure 5.

paleogeographic evolution of the northern Lhasa terrane is schematically envisaged in three stages (1–3), subdivided in turn to seven substages (Fig. 9A–9G).

Stage 1: Remnant Clastic Sea (Aptian 1–3)

After the collision between the Qiangtang and Lhasa terranes, a seaway remained as a remnant of the Bangong Ocean that once extended to the north of the Lhasa terrane (Lai et al., 2019a).

(A) Aptian 1–2 (ca. 125–120 Ma) *remnant sea* (Fig. 9A). In the Baingoin area, shelf sandstones of the Duba Formation were derived from the uplifting Bangong suture zone and southern Qiangtang terrane since 122 Ma (Lai et al., 2019a; Li et al., 2020). In the Geren Co area, submarine fan deposition took place since 125 Ma (Zhang et al., 2011). In the Coqen basin, the Duoni Formation was deposited in fluvial and next shallow shelf environments with volcaniclastic detritus sourced from the Zenong Group (Sun et al., 2017).

(B) Aptian 3 (ca. 120–116 Ma) *shrinking remnant sea* (Fig. 9B). The Duoni Formation in the Namco, Geren Co, and Selin Co areas, as in the Duba Formation in the Baingoin area, shows a shallowing-upward shallow-marine to fluvial succession (Leeder et al., 1988; Leier et al., 2007; Zhang et al., 2011; Lai et al., 2019a). The Duoni Formation in the Namco area and Coqen basin was derived from the Zenong Group (Sun et al., 2017; Lai et al., 2019a), indicating erosion of a volcanic highland to the south. Changing depositional environments indicate that large areas of the remnant sea were now exposed, although shallow-marine conditions still existed in southern Gaize area (Sun et al., 2017). Nonmarine sediments accumulated in the Northern Nima basin since 118 Ma (DeCelles et al., 2007).

Stage 2: Expanding Carbonate Seaway (Aptian 4–Cenomanian 1)

(C) Aptian 4–Albian 1 (ca. 116–110 Ma), *nascent carbonate seaway* (Fig. 9C). The Langshan Formation started to be deposited above fluvial deposits of the Duoni Formation in the south and east (Leeder at al., 1988; Zhang et al., 2011; Sun et al., 2017; Lai et al., 2019a), documenting a major transgressive event that transformed the Northern Lhasa terrane into a carbonate seaway. The seaway was then largely a shallow lagoon-patch reef environment as indicated by microfacies analysis.

(D) Albian 2 (ca. 110–107 Ma), *slightly narrower carbonate seaway* (Fig. 9D). Langshan Formation sediments changed from lagoonal to tidal flat or deltaic in the south, indicating a regression. The Damxung conglomerate was deposited to the east of Namco Lake, documenting

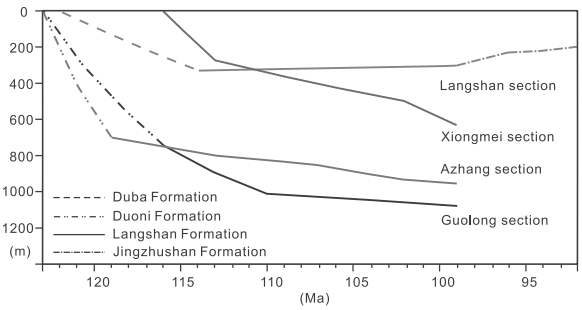

Figure 7. Tectonic subsidence of the mid-Cretaceous stratigraphic succession of the northern Lhasa terrane. Different curve types represent different formations. Data sources: Duoni Formation in the Guolong and Azhang sections (Sun et al., 2017); Duba and Jingzhushan formations (Lai et al., 2019a, 2019b); Langshan Formation in the Azhang section (Xu et al., 2020).

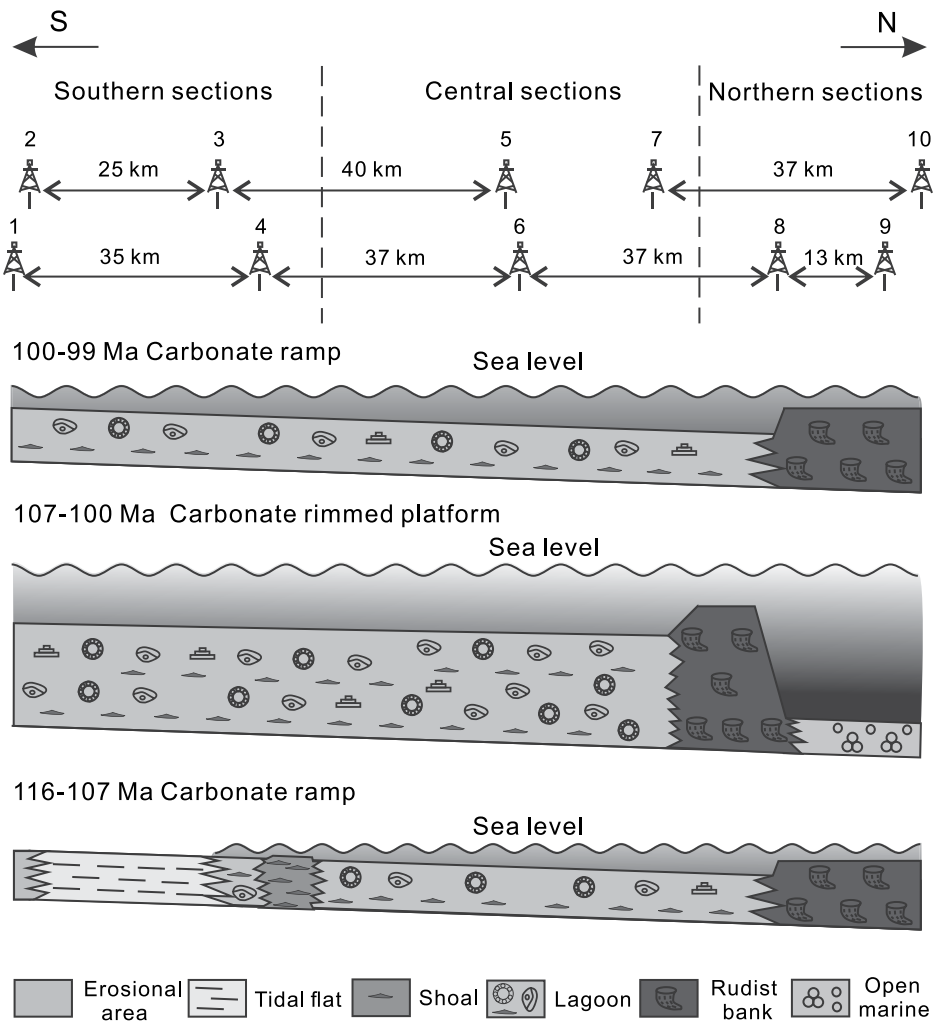

Figure 8. Facies model for the Langshan Formation. Numbers at top refer to stratigraphic sections: 1—Xiagezi; 2—Baoji; 3—Xiongmei; 4—Guolong; 5—Langshan; 6—Daya; 7—Geji; 8—Azhang; 9—Letie; 10—Zulong. Depositional environments of sections 8, 9, and 10 are after Xu et al. (2020).

the onset of tectonic uplift of northern Lhasa at its eastern part (Wang et al., 2017).

(E) Albian 3–4 (ca. 107–100 Ma), *maximum extent of the carbonate seaway* (Fig. 9E). A second gradual transgression is documented by open-marine environments established since 107 Ma in the northern Gaize-Gegyai area, whereas tidal flat deposits were overlain by shallow-lagoonal limestones around 102 Ma in the Namco area. The maximum distribution of carbonates is documented when lagoonal limestones overlaid the volcanic rocks of the Zenong Group to the south of Coqen (Xiagezi section). In the southern Nima basin, instead, non-marine deposits occur since 106 Ma (DeCelles et al., 2007).

(F) Cenomanian 1 (ca. 100–99 Ma), *disappearance of open-marine deposits* (Fig. 9F). Microfacies analysis indicates that the seaway was now a shallow-lagoon and rudist-bank environment (Xu et al., 2020), deeper areas having been filled by rudist debris.

Stage 3: Closure of Carbonate Seaway (Early Cenomanian to Turonian)

(G) Early Cenomanian to Turonian (ca. 99–92 Ma), *end of carbonate sedimentation* (Fig. 9G). Deposition of the Langshan Formation ceased in most areas during the Early Cenomanian (ca. 99–96 Ma), although a residual sea persisted in the northern Gegyai area as documented by marine deposits (Tangza Formation) of Cenomanian age (ca. 100–94 Ma) (Ye at al., 2019). The seaway disappeared completely around Turonian time (ca. 94–92 Ma), when the Jingzhushan and Daxiong formations indicate tectonic inversion with extensive erosion of Langshan carbonates.

Factors Controlling the Paleogeographic Evolution of Northern Lhasa

In this section, we shall discuss the role played by different potential factors that controlled the paleogeographic evolution of northern Lhasa during the three stages illustrated in the previous section, i.e., remnant sea during Aptian 1–3 (ca. 125–116 Ma), expanded carbonate seaway during Aptian 4–Cenomanian 1 (ca. 116–99 Ma), and closure of the carbonate seaway during the Early Cenomanian-Turonian (ca. 99−92 Ma). Because shortening and uplift are widely accepted as the principal causes for basin inversion and termination of the carbonate seaway in the northern Lhasa (Kapp et al., 2003, 2007; Volkmer et al., 2014; Sun et al., 2015a; Lai et al., 2019b), we focus here on the earlier and more controversial transition from clastic remnant sea to carbonate seaway. Two main scenarios have been envisaged: (1) deepening caused by accelerated tectonic subsidence associated with flexure, extension, or subduction (DeCelles et al., 2007; Zhang et al., 2004; Zhu et al., 2016); and (2) deepening caused by eustatic rise (Leeder et al., 1988; Zhang et al., 2011).

During stage 1, tectonic subsidence is at maximum both in the north and south of the northern Lhasa terrane (107–175 m/m.y.), although moderate in the central region (~42 m/m.y.) (Fig. 7). During stage 2, subsidence rates are markedly reduced to 13–37 m/m.y., indicating a more

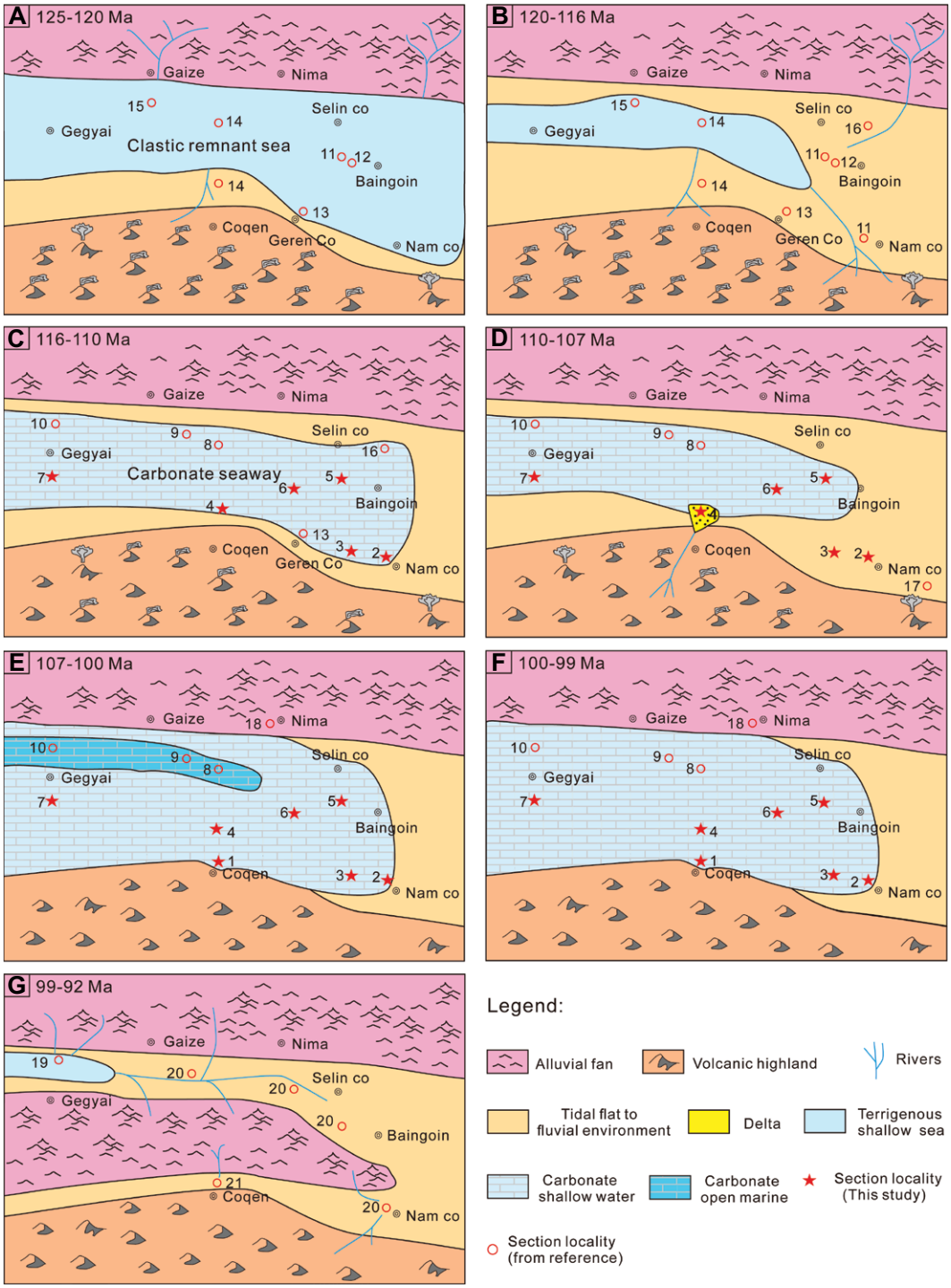

Figure 9. Mid-Cretaceous paleogeographic evolution of the northern Lhasa terrane subdivided into three stages and seven substages: remnant clastic sea (A–B), expanding carbonate seaway (C–F) and closure of carbonate seaway (G). Numbers in each panel indicate stratigraphic sections. Data sources: sections 1–7 (this study); section 8–10 (Xu et al., 2020); section 11 (Lai et al., 2019a); section 12 (Leier et al., 2007); section 13 (Zhang et al., 2011); section 14 (Sun et al., 2017); section 15 (Li et al., 2020); section 16 (Leeder et al., 1988); section 17 (Wang et al., 2017); section 18 (DeCelles et al., 2007); section 19 (Ye et al., 2019); section 20 (Lai et al., 2019b); section 21 (Sun et al., 2015a).

stable tectonic environment than during stage 1. If our assumptions and calculations are correct, then tectonic activity cannot account for increased water depth between stage 1 and stage 2.

The extensional model had been invoked to interpret this transition (Zhang et al., 2004). In this scenario, the concave-upward shape of the tectonic-subsidence curve (Fig. 7) would correspond to the stretching phase of rapid subsidence characterizing stage 1, followed by exponentially-decreasing thermal subsidence (stage 2) (Einsele, 2000).

Such an extensional-basin model is, however, contradicted by several observations. (1) During stages 1 and 2, few small-scale extensional structures have been recognized (Zhang et al., 2004). Compressional tectonics is better documented, for instance by activity along the Baingoin (Ding and Lai, 2003) and Shiquanhe-Gaize-Amdo thrusts (Kapp et al., 2007; Volkmer et al., 2014). (2) In extensional basins, the stratigraphic succession is expected to display a deepening-upward trend (Ravnås and Steel, 1998; Martins-Neto and Catuneanu, 2010). Conversely, a clear shallowing-upward trend characterizes the stage 1 of rapid subsidence (Duoni and Duba formations) (Leier et al., 2007; Zhang et al.,

2011; Lai et al., 2019a). (3). Foreland basins may also display a tectonic-subsidence curve with concave-upward shape during the transition from the thrusting phase to the quiescent phase (Flemings and Jordan, 1990).

Subsidence caused by northward subduction of Neotethyan lithosphere has also been proposed to explain this transition concurrent with widening of the seaway (Leier et al., 2007; DeCelles et al., 2007). In this scenario, however, tectonic subsidence should increase toward the subduction zone (Burgess and Moresi, 1999), but the thickness of the Langshan Formation does not show such a trend from north to south. As mentioned above, no accelerated tectonic subsidence is observed between stage 1 and stage 2, and we can thus exclude subduction-related subsidence as a main driving mechanism.

During the Cretaceous, the long-term global eustatic curve is seen to have changed from falling to slow rising since Aptian 4 (ca. 116 Ma) (Fig. 10) (Miller et al., 2005; Haq, 2014). This coincides with the first transgression event that marked the beginning of stage 2 (expanded carbonate seaway). At about Albian 2 time (ca. 107 Ma), corresponding to the second transgression event recorded by maximum spread of Langshan Formation carbonates and open-marine deposits, the rate of eustatic rise is envisaged to have reached its maximum (Fig. 10). During this second transgression, the Langshan Formation also changed from carbonate ramp to rimmed platform and then back to ramp, a transition that may have been controlled by eustasy.

During Aptian 4–Albian 2 intervals (ca. 116–107 Ma), carbonate production across the seaway kept up with slow eustatic rise (Fig. 10), resulting in a northward deepening ramp. In contrast, during Albian 3–Albian 4 (ca. 107–100 Ma), eustatic rise was too rapid (Fig. 10) for carbonate production to keep up in the entire seaway, resulting in local drowning and transition to open-marine basinal deposits. The carbonate-production rate remained locally high enough to compensate for rapidly rising sea level, and rudist banks formed a rim around the open-marine deposits, resulting in a rimmed platform relief. During Cenomanian 1 (ca. 100–99 Ma), eustatic rise slowed down (Fig. 10) and carbonate production exceeded the rate of sea-level rise, resulting in highstand shedding and filling of the basin with ramp geometry.

Similar transitions from ramp to rimmed platform, and then back to ramp, have been widely documented in Cretaceous carbonate strata of the Arabian passive margin, where eustasy was also considered to be a major controlling factor (van Buchem et al., 2002; Droste, 2010; Razin et al., 2010, 2017). The correspondence observed between facies distributions and inferred long-term global sea-level curves supports eustatic control on the transition from clastic remnant sea to the initial establishment and subsequent evolution of the Langshan carbonate seaway.

A notable reduction in width of the carbonate seaway took place between Albian 1 and Albian 3 intervals (ca. 113–107 Ma), during continuing rise of global sea level (Fig. 10). This regressive trend is documented only in southern stratigraphic sections. In the Guolong section, deltaic clastics were deposited in a relative short interval during Albian 1 (between ca. 113 and ca. 110 Ma), which corresponds to the activity of the Shibaluo thrust in the same area (Murphy et al., 1997). Local erosion feeding the progradation of a delta may thus be ascribed to tectonic control. In the Baoji and Xiongmei sections, clastic sediments were deposited in tidal flats between Albian 2 and Albian 3 (ca. 110–102 Ma), a terrigenous episode that can be ascribed to either tectonic uplift of eastern northern Lhasa, documented by coeval deposition of the Damxung conglomerate (Wang et al., 2017) or possibly to climatic influence. Although our data are insufficient to discriminate between these diverse possible controls, the general stratigraphic trend is best interpreted as largely affected by eustatic sea-level change.

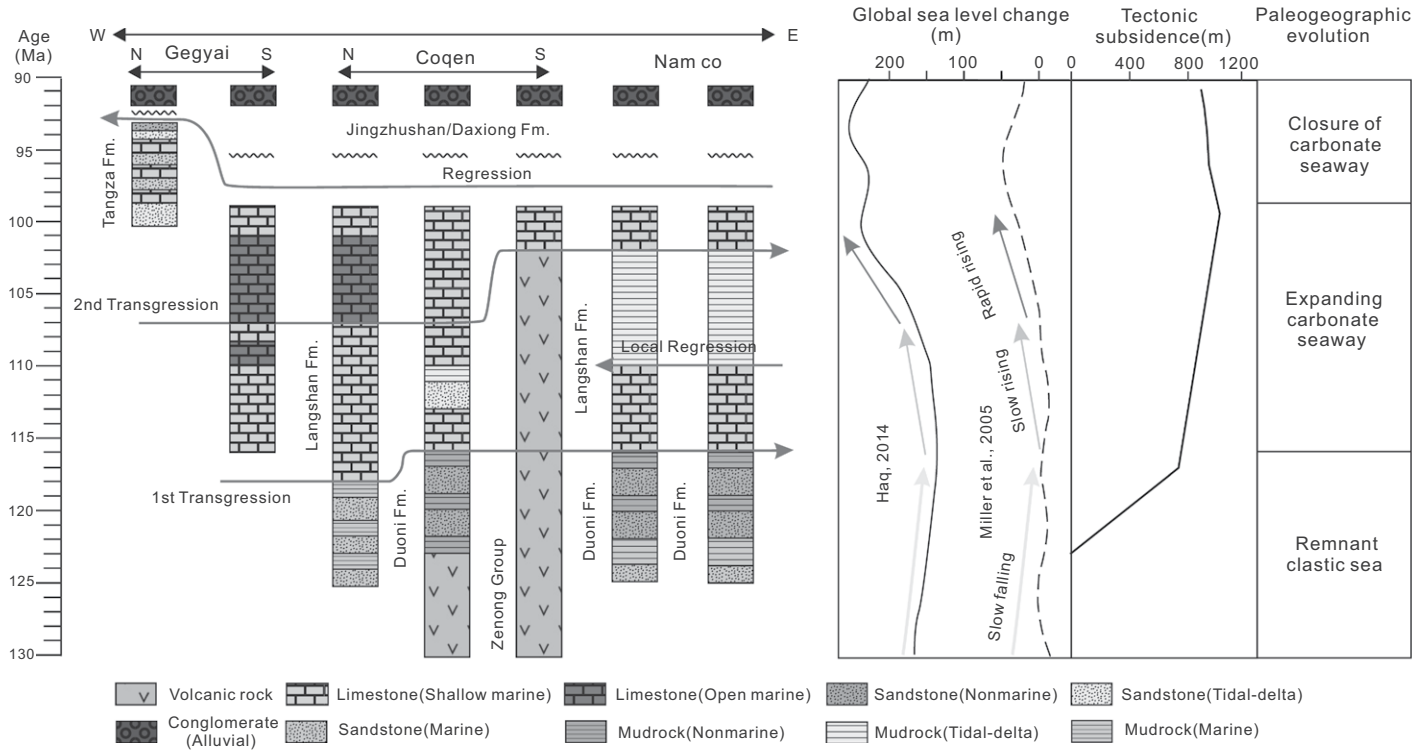

Figure 10. Stratigraphy and facies comparison among Cretaceous basins on the northern Lhasa terrane. Data sources: Duoni Formation in Baingoin Basin (Lai et al., 2019a) and Selin Co Basin (Zhang et al., 2011); Duoni Formation and Zenong Group in Coqen Basin (Sun et al., 2015a, 2017); Tangza Formation in Gegyai area (Ye et al., 2019).

Thick and Basin-Wide Carbonate Accumulation on Northern Lhasa

Carbonate accumulation implies high carbonate production and preservation and low terrigenous input (Einsele, 2000). In sedimentary basins adjacent to orogenic belts, intense tectonic activity and erosion generally produces large volumes of terrigenous detritus which tend to suppress and dilute carbonate production (Wilson, 1975).

To the north of the Lhasa terrane, the Bangong suture zone was formed, uplifted, and eroded far earlier than deposition of the Langshan Formation (DeCelles et al., 2007; Kapp et al., 2007; Ma et al., 2020). Abundant terrigenous detritus was being shed southward from the suture zone and accumulated as the Duba Formation in the northern part of the Northern Lhasa terrane (Lai et al., 2019a; Li et al., 2020), while volcaniclastic detritus largely derived from the Zenong Group accumulated as Duoni Formation in the southern part of the Northern Lhasa terrane (Fig. 11A). At this time (Aptian 1–3), only few carbonate sediments were deposited in the central part of the basin. Subsequently (Aptian 4–Cenomanian 1), the siliciclastic Duoni and Duba formations were replaced by the widespread limestones of the Langshan Formation.

The transition between the Duoni/Duba clastics and the Langshan carbonates represents a major marine transgression, as indicated by facies change from fluvial clastic to shallow-marine carbonate deposits across most northern Lhasa (Figs. 9B and 9C). During initial expansion of the carbonate seaway (Aptian 4–Albian1, ca. 116–110 Ma), clastic supply did not cease completely, and the Duoni/Duba clastics continued to be deposited until to the Albian 1–2 (ca. 110–108 Ma) in marginal areas (Lai et al., 2019a). During transgression, terrigenous detritus was thus confined along the margin of the seaway, leaving carbonate deposition to flourish in the relatively clean waters of the underfilled seaway. Continuing sea-level rise led carbonate deposits to finally occupy the whole of northern Lhasa (Figs. 9D–9F).

The character of the faunas also contributed to the basin-wide distribution of carbonates. Orbitolinids and rudists, the typical biota of the Langshan Formation, are adapted to more turbid water than corals (Wilson, 1975; Gili et al., 1995; Pittet et al., 2002). Orbitolinids can coexist with even abundant terrigenous supply and also use terrigenous clast to build their test (as shown in strata analogous to our MF 16 and by Pittet et al., 2002). Carbonate production by orbitolinids even in turbid waters close to the margin of the seaway may have significantly contributed to the progressive coastward expansion of carbonate deposits (Fig. 11B).

The thickness of the Langshan carbonates (~800–1200 m) cannot be explained solely by eustatic changes. The magnitude of eustatic rise between the late Aptian and the Cenomanian is estimated as ~55–115 m (Miller et al., 2005; Haq, 2014). In the Airy isostasy model—assuming densities of sea water, sediment, and asthenosphere to be 1.03 g/cm^3, 2.4 g/cm^3, and 3.3 g/cm^3 respectively (Einsele, 2000)—such a sea-level rise would induce a maximum accommodation space of ~140–290 m. Thus, additional tectonically driven subsidence (~15–40 m/m.y. as calculated by backstripping, Fig. 7) are required to compatible with the thickness of Langshan carbonate accumulation.

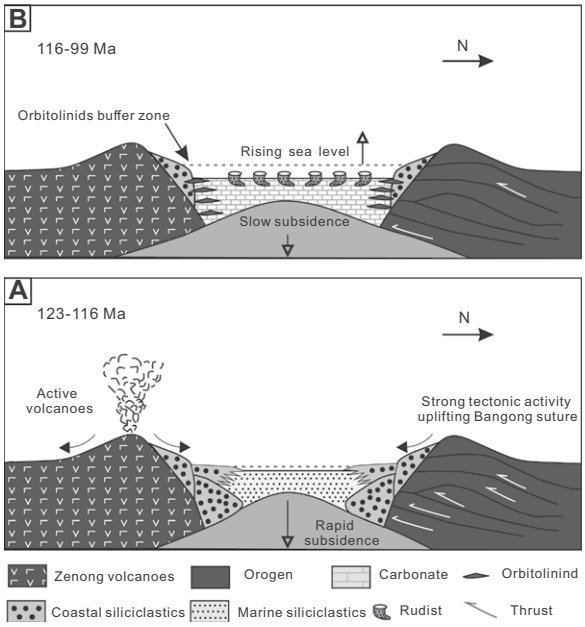

Figure 11. Controls on carbonate deposition on the northern Lhasa terrane. (A) Terrigenous supply from the Zenong volcanic rocks and Bangong suture zone suppresses carbonate production. (B) Rising sea-level and orbitolinids trap terrigenous detritus in marginal areas, leaving clean waters for carbonate deposition, where slow tectonic subsidence provides accommodation for carbonates.

The thick and basin-wide carbonate accumulation that occurred at mid-Cretaceous times in the northern Lhasa terrane is thus interpreted as mainly controlled by eustatic changes, combined with long-term slow tectonic subsidence and favored by the tolerance of the mid-Cretaceous fauna to relatively turbid water (Fig. 11B).

Three examples can be compared to this study. The best one is represented by the Arabian/Persian Gulf foreland basin, which was entirely exposed subaerially during the last glacial maximum (21,000~20,000 years ago; Lambeck, 1996; Garzanti et al., 2013). During the Holocene global sea-level rise, the Gulf was reoccupied by seawater and carbonate sedimentation became widespread across the basin (Uchupi et al., 1999). Because of arid climate, no terrigenous detritus was being supplied from Arabia, very little from the largely carbonate Zagros Mountains in Iran, and even orogenic detritus from Anatolia and the Zagros farther north was mostly trapped inland in southern Mesopotamia (Garzanti et al., 2016).

Another example is provided by the Carboniferous Appalachian foreland basin. Terrigenous deposition during the middle Mississippian was followed by a stage when relative tectonic quiescence and sea-level rise led to reduced influx of terrigenous detritus and accumulation of shallow-water carbonates throughout the basin (Ettensohn, 1994). This stage, however, lasted only ~3 m.y., and ~80-m-thick carbonates were buried by terrigenous sediment in the latest Mississippian (Ettensohn, 1994; Ryder et al., 2015)

The third example is provided by Miocene carbonate strata of the central Great Barrier Reef in the Papua-New Guinea foreland basin. Between the middle Eocene and the early Oligocene, Papua New Guinea was a passive margin with limited distribution of up to 0.5-km-thick carbonate rocks (Pigram et al., 1989). Subsequently, between the latest Oligocene and the earliest Pliocene, 1.2-km-thick tropical carbonates were deposited during long-term relative sea-level rise (Davies et al., 1989; Pigram et al., 1989). The distribution of tropical carbonates, however, was limited to the southern part of the basin, largely because the major carbonate producers were corals (Davies et al., 1989). Corals flourish only in clear water, and terrigenous detritus unhampered by humid climate restricted carbonate accumulation to the margin of the foreland basin (Davies et al., 1989; Pigram et al., 1989).

Eustatic rise, long-term tectonic subsidence, arid climate, and tolerance of carbonate biota to turbid waters are thus all necessary concurrent preconditions to foster carbonate accumulation in a foreland basin. These conditions must all be met for thick and basin-wide thick carbonates to accumulate basin-wide near an active orogenic belt. Such a strict combination of requirements

explains why basin-wide and thick carbonate accumulations rarely occur in orogenic settings.

CONCLUSIONS

Detailed sedimentological and biostratigraphic analysis of the Langshan Formation deposited on the Northern Lhasa terrane allowed identification of 19 microfacies, corresponding to five distinct depositional environments (delta plain, tidal flat, shallow lagoon, open lagoon, and patch reef). Biostratigraphic and geochronological evidence indicates that the Langshan Formation was deposited between Late Aptian and Early Cenomanian.

By combining new stratigraphic and microfacies observations with data from the literature, three stages have been identified in the mid-Cretaceous paleogeographic evolution of the northern Lhasa terrane. Stage 1 (remnant clastic sea; Early Aptian to early Late Aptian, ca. 125–116 Ma) documents a regressive trend. During stage 2, transgression and widespread carbonate deposition were favored by slow subsidence and reduced tectonic activity (expanding carbonate seaway; latest Aptian to earliest Cenomanian, ca. 116–99 Ma). During stage 3 (closure of the carbonate seaway; Early Cenomanian to Turonian, ca. 99–92 Ma), carbonate sedimentation came to an end owing to tectonic uplift of northern Lhasa. Reduced tectonic subsidence and comparison with the global sea-level curve suggests that paleogeographic evolution during stage 2 was largely controlled by eustatic changes. Thick and basin-wide carbonate accumulation in orogenic settings require a suitable combination of sea-level, long-term tectonic subsidence, arid climate, as well as tolerance of carbonate-producing organisms to relatively turbid sea waters.

ACKNOWLEDGMENTS

We thank Jiapeng Ye and Weiwei Xue for their help in the field, and Juan Li and Zhong Han for their assistance in the analysis of thin sections and tectonic subsidence. We are deeply grateful to the editor, to Andrew Leier, and one anonymous reviewer for their constructive comments and advice. This study was financially supported by National Natural Science Foundation of China (41525007, 91755209, 41888101).

REFERENCES CITED

Allen, P.A., and Allen, J.R., 2005, Basin Analysis: Principles and Applications: Oxford, UK, Wiley-Blackwell, 451 p.

Bachmann, M., and Hirsch, F., 2006, Lower Cretaceous carbonate platform of the eastern Levant (Galilee and the Golan Heights): stratigraphy and second-order sea-level change: Cretaceous Research, v. 27, no. 4, p. 487–512, https://doi.org/10.1016/j.cretres.2005.09.003.

Banner, F.T., and Simmons, M.D., 1994, Calcareous algae and foraminifera as water-depth indicators: an example from the Early Cretaceous carbonates of northeast Arabia, *in* Simmons, M.D., ed., Micropalaeontology and Hydrocarbon Exploration in the Middle East: British Micropalaeontological Society Publications Series, p. 243–252.

Bosence, D., 2005, A genetic classification of carbonate platforms based on their basinal and tectonic settings in the Cenozoic: Sedimentary Geology, v. 175, no. 1, p. 49–72, https://doi.org/10.1016/j.sedgeo.2004.12.030.

BouDagher-Fadel, M.K., Hu, X.M., Price, G.D., Sun, G.Y., Wang, J.G., and An, W., 2017, Foraminiferal biostratigraphy and palaeoenvironmental analysis of the Mid-Cretaceous limestones in the southern Tibetan Plateau: Journal of Foraminiferal Research, v. 47, no. 2, p. 188–207, https://doi.org/10.2113/gsjfr.47.2.188.

Busby, C.J., and Ingersoll, R.V., 1995, Tectonics of Sedimentary Basins: Oxford, Blackwell Science, 579 p.

Burgess, P.M., and Moresi, L.N., 1999, Modelling rates and distribution of subsidence due to dynamic topography over subducting slabs: is it possible to identify dynamic topography from ancient strata?: Basin Research, v. 11, no. 4, p. 305–314, https://doi.org/10.1046/j.1365-2117.1999.00102.x.

Davies, P.J., Symonds, P.A., Feary, D.A., Pigram, C.J., Crevello, P.D., Wilson, J.L., Sarg, J.F., and Read, J.F., 1989, The Evolution of the Carbonate Platforms of Northeast Australia, *in* Crevello, P.D., Wilson, J.L., Sarg, J.F., and Read J.F., eds., Controls on Carbonate Platforms and Basin Development: SEPM Society for Sedimentary Geology, Special Publication 44, p. 233–258, https://doi.org/10.2110/pec.89.44.0233.

Davies, R.B., Casey, D.M., Horbury, A.D., Sharland, P.R., and Simmons, M.D., 2002, Early to mid-Cretaceous mixed carbonate-clastic shelfal systems: examples, issues and models from the Arabian Plate: GeoArabia, v. 7, no. 3, p. 541–598.

Dewey, J.F., Shackleton, R.M., Chang, C.F., and Sun, Y.Y., 1988, The tectonic evolution of the Tibetan Plateau: Royal Society of London Philosophical Transactions, ser. A: Mathematical and Physical Sciences, v. 327, p. 379–413, https://doi.org/10.1098/rsta.1988.0135.

DeCelles, P.G., Kapp, P., Ding, L., and Gehrels, G.E., 2007, Late Cretaceous to mid-Tertiary basin evolution in the central Tibetan Plateau: Changing environments in response to tectonic partitioning, aridification, and regional elevation gain: Geological Society of America Bulletin, v. 119, p. 654–680, https://doi.org/10.1130/B26074.1.

Ding, L., and Lai, Q., 2003, New geological evidence of crustal thickening in the Gangdese block prior to the Indo-Asian collision: Chinese Science Bulletin, v. 48, p. 1604–1610, https://doi.org/10.1007/BF03183969.

Di Stefano, P., and Ruberti, D., 2000, Cenomanian rudist-dominated shelf-margin limestones from the panormide carbonate platform (Sicily, Italy): Facies analysis and sequence stratigraphy: Facies, v. 42, no. 1, p. 133–160, https://doi.org/10.1007/BF02562570.

Dorobek, S.L., 1995, Synorogenic carbonate platforms and reefs in foreland basins, *in* Dorobek, S.L., and Ross, G.M., eds., Controls on Stratigraphic Evolution and Platform/Reef Morphology, Stratigraphic Evolution of Foreland Basins: SEPM Society for Sedimentary Geology, Special Publication 52, p. 127–147, https://doi.org/10.2110/pec.95.52.0127.

Droste, H., 2010, High-resolution seismic stratigraphy of the Shu'aiba and Natih formations in the Sultanate of Oman: implications for Cretaceous epeiric carbonate platform systems, *in* van Buchem, F.S.P., Gerdes, K.D., and Esteban, M., eds., Mesozoic and Cenozoic Carbonate Systems of the Mediterranean and the Middle East: Stratigraphic and Diagenetic Reference Models: Geological Society, London, Special Publication 329, p. 187–218, https://doi.org/10.1144/SP329.7.

Dunham, R.J., 1962, Classification of carbonate rocks according to depositional textures, *in* Ham, W.E., ed., Classification of Carbonate Rocks: American Association of Petroleum Geologists Memoir 1, p. 108–121.

Einsele, G., 2000, Sedimentary Basins: Evolution, Facies, and Sediment Budget (2nd ed.): Springer Science & Business Media, 792 p, https://doi.org/10.1007/978-3-662-04029-4.

Embry, A.F., and Klovan, J.E., 1971, A late Devonian reef tract on Northeastern Banks Island, N.W.T: Bulletin of Canadian Petroleum Geology, v. 19, no. 4, p. 730–781.

Ettensohn, F.R., 1994, Tectonic control on the formation and cyclicity of major Appalachian unconformities and associated stratigraphic sequences, *in* Dennison, J.M., and Ettensohn, F.R., eds., Tectonic and eustatic controls on sedimentary cycles: Society for Sedimentary Geology (SEPM) Concepts in Sedimentology and Paleontology, v. 4, p. 217–242, https://doi.org/10.2110/csp.94.04.0217.

Fan, J.-J., Li, C., Xie, C.-M., and Wang, M., 2014, Petrology, geochemistry, and geochronology of the Zhonggang ocean island, northern Tibet: implications for the evolution of the Banggongco–Nujiang oceanic arm of the Neo-Tethys: International Geology Review, v. 56, no. 12, p. 1504–1520, https://doi.org/10.1080/00206814.2014.947639.

Fernández-Mendiola, P.A., Mendicoa, J., Hernandez, S., Owen, H.G., and García-Mondéjar, J., 2013, A facies model for an Early Aptian carbonate platform (Zamaia, Spain): Facies, v. 59, no. 3, p. 529–558, https://doi.org/10.1007/s10347-012-0315-3.

Flemings, P.B., and Jordan, T.E., 1990, Stratigraphic modeling of foreland basins: Interpreting thrust deformation and lithosphere rheology: Geology, v. 18, p. 430–434, https://doi.org/10.1130/0091-7613(1990)018<0430:SMOFBI>2.3.CO;2.

Flügel, E., 2010, Microfacies of Carbonate Rocks: Analysis, Interpretation and Application (2nd ed.): Berlin, Springer-Verlag, 924 p., https://doi.org/10.1007/978-3-642-03796-2.

Garzanti, E., Vermeesch, P., Andò, S., Vezzoli, G., Valagussa, M., Allen, K., Khadi, K.A., and Al-Juboury, I.A., 2013, Provenance and recycling of Arabian desert sand: Earth-Science Reviews, v. 120, p. 1–19, https://doi.org/10.1016/j.earscirev.2013.01.005.

Garzanti, E., Al-Juboury, A.I., Zoleikhaei, Y., Vermeesch, P., Jotheri, J., Akkoca, D.B., Allen, M., Andò, S., Limonta, M., Padoan, M., Resentini, A., Rittner, M., and Vezzoli, G., 2016, The Euphrates-Tigris-Karun river system: provenance, recycling and dispersal of quartz-poor foreland-basin sediments in arid climate: Earth-Science Reviews, v. 162, p. 107–128, https://doi.org/10.1016/j.earscirev.2016.09.009.

Ghabeishavi, A., Vaziri-Moghaddam, H., Taheri, A., and Taati, F., 2010, Microfacies and depositional environment of the Cenomanian of the Bangestan anticline, SW Iran: Journal of Asian Earth Sciences, v. 37, no. 3, p. 275–285, https://doi.org/10.1016/j.jseaes.2009.08.014.

Gili, E., Masse, J.-P., and Skelton, P.W., 1995, Rudists as gregarious sediment-dwellers, not reef-builders, on Cretaceous carbonate platforms: Palaeogeography, Palaeoclimatology, Palaeoecology, v. 118, p. 245–267, https://doi.org/10.1016/0031-0182(95)00006-X.

Girardeau, J., Marcoux, J., Allègre, C.J., Bassoullet, J.P., Youking, T., Xuchang, X., Yougong, Z., and Xibin, W., 1984, Tectonic environment and geodynamic significance of the Neo-Cimmerian Donqiao ophiolite, Bangong-Nujiang suture zone, Tibet: Nature, v. 307, no. 5946, p. 27–31, https://doi.org/10.1038/307027a0.

Gradstein, F.M., Ogg, J.G., Schmitz, M.D., and Ogg, G.M., 2012, The Geological Time Scale 2012: Elsevier, Amsterdam, 1176 p, https://doi.org/10.1016/C2011-1-08249-8.

Haq, B.U., 2014, Cretaceous eustasy revisited: Global and Planetary Change, v. 113, p. 44–58, https://doi.org/10.1016/j.gloplacha.2013.12.007.

James, N.P., and Jones, B., 2015, Origin of carbonate sedimentary rocks: John Wiley & Sons, 464 p.

Jordan, C.F., Connolly, T.C., and Vest, H.A., 1985, Middle Cretaceous Carbonates of the Mishrif Formation, Fateh Field, Offshore Dubai, U.A.E, *in* Roehl, P.O., and Choquette, P.W., eds., Carbonate Petroleum Reservoirs: Casebooks in Earth Sciences: New York, New York, Springer, https://doi.org/10.1007/978-1-4612-5040-1_27 .

Kapp, P., and DeCelles, P.G., 2019, Mesozoic–Cenozoic geological evolution of the Himalayan-Tibetan orogen and working tectonic hypotheses: American Journal of Science, v. 319, no. 3, p. 159–254, https://doi.org/10.2475/03.2019.01.

Kapp, P., Murphy, M.A., Yin, A., Harrison, T.M., Ding, L., and Guo, J., 2003, Mesozoic and Cenozoic tectonic evolution of the Shiquanhe area of western Tibet: Tectonics, v. 22, no. 4, p. 3-1–3-25, https://doi.org/10.1029/2001TC001332.

Kapp, P., DeCelles, P.G., Leier, A.L., Fabijanic, J.M., He, S., Pullen, A., and Gehrels, G.E., 2007, The Gangdese retroarc thrust belt revealed: GSA Today, v. 17, no. 7, p. 4–9, https://doi.org/10.1130/GSAT01707A.1.

Kaya, M.Y., and Altıner, D., 2015, Microencrusters from the Upper Jurassic–Lower Cretaceous İnaltı Formation (Central Pontides, Turkey): remarks on the development of reefal/peri-reefal facies: Facies, v. 61, no. 4, p. 18, https://doi.org/10.1007/s10347-015-0445-5.

Lai, W., Hu, X., Garzanti, E., Xu, Y., Ma, A., and Li, W., 2019a, Early Cretaceous sedimentary evolution of the northern Lhasa terrane and the timing of initial Lhasa-Qiangtang collision: Gondwana Research, v. 73, p. 136–152, https://doi.org/10.1016/j.gr.2019.03.016.

Lai, W., Hu, X.M., Garzanti, E., Sun, G.Y., Garzione, C.N., BouDagher-Fadel, M., and Ma, A.L., 2019b, Initial growth of the northern Lhasaplano in the early Late Cretaceous (ca. 92 Ma): Geological Society of America Bulletin, v. 131, p. 1823–1836, https://doi.org/10.1130/B35124.1.

Lambeck, K., 1996, Shoreline reconstructions for the Persian Gulf since the last glacial maximum: Earth and Planetary Science Letters, v. 142, no. 1, p. 43–57, https://doi.org/10.1016/0012-821X(96)00069-6.

Leeder, M.R., Smith, A.B., and Jixiang, Y., 1988, Sedimentology, palaeoecology and palaeoenvironmental evolution of the 1985 Lhasa to Golmud Geotraverse: Royal Society of London Philosophical Transactions, ser. A: Mathematical and Physical Sciences, v. 327, p. 107–143, https://doi.org/10.1098/rsta.1988.0123.

Leier, A.L., DeCelles, P.G., Kapp, P., and Gehrels, G.E., 2007, Lower Cretaceous strata in the Lhasa Terrane, Tibet, with implications for understanding the early tectonic history of the Tibetan Plateau: Journal of Sedimentary Research, v. 77, p. 809–825, https://doi.org/10.2110/jsr.2007.078.

Li, S., Yin, C., Guilmette, C., Ding, L., and Zhang, J., 2019, Birth and demise of the Bangong-Nujiang Tethyan Ocean: A review from the Gerze area of central Tibet: Earth-Science Reviews, v. 198, 102907, https://doi.org/10.1016/j.earscirev.2019.102907.

Li, S., Yin, C., Ding, L., Guilmette, C., Zhang, J., Yue, Y., and Baral, U., 2020, Provenance of Lower Cretaceous sedimentary rocks in the northern margin of the Lhasa terrane, Tibet: Implications for the timing of the Lhasa-Qiangtang collision: Journal of Asian Earth Sciences, v. 190, 104162, https://doi.org/10.1016/j.jseaes.2019.104162.

Martins-Neto, M.A., and Catuneanu, O., 2010, Rift sequence stratigraphy: Marine and Petroleum Geology, v. 27, p. 247–253, https://doi.org/10.1016/j.marpetgeo.2009.08.001.

Ma, A.L., Hu, X.M., Garzanti, E., Han, Z., and Lai, W., 2017, Sedimentary and tectonic evolution of the southern Qiangtang basin: Implications for the Lhasa-Qiangtang collision timing: Journal of Geophysical Research. Solid Earth, v. 122, no. 7, p. 4790–4813, https://doi.org/10.1002/2017JB014211.

Ma, A.L., Hu, X.M., Kapp, P., BouDagher-Fadel, M., and Lai, W., 2020, Pre-Oxfordian (>163 Ma) Ophiolite Obduction in Central Tibet: Geophysical Research Letters, v. 47, https://doi.org/10.1029/2019GL086650.

Masse, J.P., 1992, The Lower Cretaceous Mesogean benthic ecosystems: palaeoecologic aspects and palaeobiogeographic implications: Palaeogeography, Palaeoclimatology, Palaeoecology, v. 91, no. 3, p. 331–345, https://doi.org/10.1016/0031-0182(92)90075-G.

Masse, J.-P., Philip, J., and Toomey, D.F., 1981, Cretaceous Coral-Rudist Buildups of France, *in* Toomey, D. F., ed., European Fossil Reef Models: SEPM Society for Sedimentary Geology, Special Publication 30, p. 399–426, http://doi.org/10.2110/pec.81.30.0399.

Miller, K.G., Kominz, M.A., Browning, J.V., Wright, J.D., Mountain, G.S., Katz, M.E., Sugarman, P.J., Cramer, B.S., Christie-Blick, N., and Pekar, S.F., 2005, The Phanerozoic Record of Global Sea-Level Change: Science, v. 310, no. 5752, p. 1293–1298, https://doi.org/10.1126/science.1116412.

Murphy, M.A., Yin, A., Harrison, T.M., Dürr, S.B., Chen, Z., Ryerson, F.J., Kidd, W.S.F., Wang, X., and Xiao, Z., 1997, Did the Indo-Asian collision alone create the Tibetan plateau?: Geology, v. 25, p. 719–722, https://doi.org/10.1130/0091-7613(1997)025<0719:DTIACA>2.3.CO;2.

Pan, G.T., Ding, J., Yao, D.S., and Wang, L.Q., 2004, Guide Book of 1:1,500,000 Geologic Map of the QinghaiXizang (Tibet) Plateau and Adjacent Areas: Chengdu, China, Cartographic Publishing House, 148 p.

Pigram, C.J., Davies, P.J., Feary, D.A., and Symonds, P.A., 1989, Tectonic controls on carbonate platform evolution in southern Papua New Guinea: Passive margin to foreland basin: Geology, v. 17, no. 3, p. 199–202, https://doi.org/10.1130/0091-7613(1989)017<0199:TCOCPE>2.3.CO;2.

Pittet, B., Van Buchem, F.S.P., Hillgärtner, H., Razin, P., Grötsch, J., and Droste, H., 2002, Ecological succession, palaeoenvironmental change, and depositional sequences of Barremian–Aptian shallow-water carbonates in northern Oman: Sedimentology, v. 49, no. 3, p. 555–581, https://doi.org/10.1046/j.1365-3091.2002.00460.x.

Rao, X., Skelton, P.W., Sha, J., Cai, H., and Iba, Y., 2015, Mid-Cretaceous rudists (Bivalvia: Hippuritida) from the Langshan Formation, Lhasa block, Tibet: Papers in Palaeontology, v. 1, no. 4, p. 401–424, https://doi.org/10.1002/spp2.1019.

Rao, X., Skelton, P.W., Sano, S.i., Zhang, Y., Zhang, Y., Pan, Y., Cai, H., Peng, B., Zhang, T., and Ma, Z., 2020, Shajia, a new genus of polyconitid rudist from the Langshan Formation of the Lhasa block, Tibet, and its palaeogeographical implications: Cretaceous Research, v. 105, 104151, https://doi.org/10.1016/j.cretres.2019.05.009.

Ravnås, R., and Steel, R.J., 1998, Architecture of marine rift-basin successions: The American Association of Petroleum Geologists Bulletin, v. 82, p. 110–146, https://doi.org/10.1306/1D9BC3A9-172D-11D7-8645000102C1865D.

Razin, P., Taati, F., and van Buchem, F.S.P., 2010, Sequence stratigraphy of Cenomanian Turonian carbonate platform margins (Sarvak Formation) in the High Zagros, SW Iran: an outcrop reference model for the Arabian Plate, *in* van Buchem, F.S.P., Gerdes, K.D., and Esteban, M., eds., Mesozoic and Cenozoic Carbonate Systems of the Mediterranean and the Middle East: Stratigraphic and Diagenetic Reference Models: Geological Society, London, Special Publication 329, p. 187–218, https://doi.org/10.1144/SP329.9.

Razin, P., Grélaud, C., and van Buchem, F., 2017, The mid-Cretaceous Natih Formation in Oman: A model for carbonate platforms and organic-rich intrashelf basins: AAPG Bulletin, v. 101, no. 4, p. 515–522, https://doi.org/10.1306/011817DIG17030.

Ryder, R.T., Trippi, M.H., and Swezey, C.S., 2015, Geologic cross section I–I′ through the Appalachian basin from the eastern margin of the Illinois basin, Jefferson County, Kentucky, to the Valley and Ridge province, Scott County, Virginia: U.S. Geological Survey Scientific Investigations Map 3343, 2 sheets and pamphlet A, 41 p.; pamphlet B, 102 p., https://doi.org/10.3133/sim3343.

Sclater, J.G., and Christie, P.A.F., 1980, Continental stretching: An explanation of the post-mid-Cretaceous subsidence of the central North Sea basin: Journal of Geophysical Research, v. 85, p. 3711–3739, https://doi.org/10.1029/JB085iB07p03711.

Scott, R.W., Wan, X., Sha, J., and Wen, S.-X., 2010, Rudists of Tibet and the Tarim Basin, China: Significance to Requieniidae phylogeny: Journal of Paleontology, v. 84, no. 3, p. 444–465, https://doi.org/10.1666/09-137.1.

Sinclair, H.D., 1997, Tectonostratigraphic model for underfilled peripheral foreland basins: An Alpine perspective: Geological Society of America Bulletin, v. 109, p. 324–346, https://doi.org/10.1130/0016-7606(1997)109<0324:TMFUPF>2.3.CO;2.

Stein, M., Arnaud-Vanneau, A., Adatte, T., Fleitmann, D., Spangenberg, J.E., and Föllmi, K.B., 2012, Palaeoenvironmental and palaeoecological change on the northern Tethyan carbonate platform during the Late Barremian to earliest Aptian: Sedimentology, v. 59, no. 3, p. 939–963, https://doi.org/10.1111/j.1365-3091.2011.01286.x.

Sun, G., Hu, X., Sinclair, H.D., BouDagher-Fadel, M.K., and Wang, J., 2015a, Late Cretaceous evolution of the Coqen Basin (Lhasa terrane) and implications for early topographic growth on the Tibetan Plateau: Geological Society of America Bulletin, v. 127, p. 1001–1020, https://doi.org/10.1130/B31137.1.

Sun, G.Y., Hu, X.M., Zhu, D.C., Hong, W.T., Wang, J.G., and Wang, Q., 2015b, Thickened juvenile lower crust-derived ~90 Ma adakitic rocks in the central Lhasa terrane, Tibet: Lithos, v. 224–225, p. 225–239, https://doi.org/10.1016/j.lithos.2015.03.010.

Sun, G., Hu, X., and Sinclair, H.D., 2017, Early Cretaceous palaeogeographic evolution of the Coqen Basin in the Lhasa Terrane, southern Tibetan Plateau: Palaeogeography, Palaeoclimatology, Palaeoecology, v. 485, p. 101–118, https://doi.org/10.1016/j.palaeo.2017.06.006.

Uchupi, E., Swift, S.A., and Ross, D.A., 1999, Late Quaternary stratigraphy, Paleoclimate and neotectonism of the Persian (Arabian) Gulf region: Marine Geology, v. 160, no. 1, p. 1–23, https://doi.org/10.1016/S0025-3227(99)00011-0.

van Buchem, F.S., Pittet, B., Hillgärtner, H., Grötsch, J., Al Mansouri, A.I., Billing, I.M., Droste, H., and van Steenwinkel, M., 2002, High-resolution sequence stratigraphic architecture of Barremian/Aptian carbonate systems in northern Oman and the United Arab Emirates (Kharaib and Shu'aiba formations): GeoArabia, v. 7, no. 3, p. 461–500.

Volkmer, J.E., Kapp, P., Horton, B.K., Gehrels, G.E., Minervini, J.M., Ding, L., Nie, J., Horton, B.K., and Hoke, G.D., 2014, Northern Lhasa thrust belt of central Tibet: Evidence of Cretaceous–early Cenozoic shortening within a passive roof thrust system? *in* Nie, J., Horton, B.K., and Hoke, G.D., eds., Toward an Improved Understanding of Uplift Mechanisms and the Elevation History of the Tibetan Plateau: Geological Society of America Special Paper 507, p. 59–70, https://doi.org/10.1130/2014.2507(03).

Wang, J.G., Hu, X.M., Garzanti, E., Ji, W.Q., Liu, Z.C., Liu, X.C., and Wu, F.Y., 2017, Early cretaceous topographic growth of the Lhasaplano, Tibetan plateau: Constraints from the Damxung conglomerate: Journal of Geophysical Research. Solid Earth, v. 122, no. 7, p. 5748–5765, https://doi.org/10.1002/2017JB014278.

Wilson, J.L., 1975, Carbonate facies in geologic history: Springer Science & Business Media, 471 p., https://doi.org/10.1007/978-1-4612-6383-8.

Xu, Y.W., Hu, X.M., BouDagher-Fadel, M.K., Sun, G.Y., Lai, W., Li, J., and Zhang, S.J., 2020, The major Late Albian transgressive event recorded in the epeiric platform of the Langshan Formation in central Tibet, *in* Wagreich, M., Hart, M.B., Sames, B., and Yilmaz, I.O., eds., Cretaceous Climate Events and Short-Term Sea-Level Changes: Geological Society, London, Special Publication 498, p. 211–232, https://doi.org/10.1144/SP498-2019-8.

Ye, J.P., Hu, X.M., Sun, G.Y., and BouDagher-Fadel, M.K., 2019, The disappearance of the Late Cretaceous Bangong-Nujiang residual seaway constrained by youngest marine strata in Geji area, Lhasa Terrane: Chinese Science Bulletin, v. 64, no. 15, p. 1620–1636, https://doi.org/10.1360/N972018-01092.

Yu, G.M., and Wang, C.S., 1990, People's Republic of China Ministry of Geology and Mineral Resources, Geological Memoirs, Serious 3, Number 12, Sedimentary geology of the Xizang (Tibet) Tethys: Geological Publishing House, Beijing, 185 p.

Zhang, K.-J., Xia, B.-D., Wang, G.-M., Li, Y.-T., and Ye, H.-F., 2004, Early Cretaceous stratigraphy, depositional environments, sandstone provenance, and tectonic setting of central Tibet, western China: Geological Society of America Bulletin, v. 116, p. 1202–1222, https://doi.org/10.1130/B25388.1.

Zhang, Q.-H., Ding, L., Cai, F.-L., Xu, X.-X., Zhang, L.-Y., Xu, Q., and Willems, H., 2011, Early Cretaceous Gangdese retroarc foreland basin evolution in the Selin Co basin, central Tibet: evidence from sedimentology and detrital zircon geochronology, *in* Gloaguen, R., and Ratschbacher, L., eds., Growth and Collapse of the Tibetan Plateau: Geological Society, London, Special Publication 353, p. 27–44, https://doi.org/10.1144/SP353.3.

Zhu, D.-C., Li, S.-M., Cawood, P.A., Wang, Q., Zhao, Z.-D., Liu, S.-A., and Wang, L.-Q., 2016, Assembly of the Lhasa and Qiangtang terranes in central Tibet by divergent double subduction: Lithos, v. 245, p. 7–17, https://doi.org/10.1016/j.lithos.2015.06.023.

Science Editor: Rob Strachan
Associate Editor: Troy Rasbury

Manuscript Received 30 September 2020
Revised Manuscript Received 30 January 2021
Manuscript Accepted 23 February 2021

Printed in the USA